

Removing Satellite Equatorial Crossing Time Biases from the OLR and HRC Datasets

DUANE E. WALISER AND WUFENG ZHOU

Institute for Terrestrial and Planetary Atmospheres, State University of New York at Stony Brook, Stony Brook, New York

(Manuscript received 16 September 1996, in final form 22 January 1997)

ABSTRACT

The objective of this study is to examine the impacts from satellite equatorial crossing time (ECT) changes on the outgoing longwave radiation (OLR) and highly reflective cloud (HRC) datasets and to design appropriate and robust methods to remove these satellite-dependent biases. The OLR record covers the period from June 1974 to July 1996 and is on a 2.5° grid extending from 30°S to 30°N over the global Tropics. The HRC record covers the period from January 1971 to December 1987 and is on a 2° grid extending from 25°S to 25°N over the global Tropics. Rotated empirical orthogonal function analysis (REOF) is performed on both the monthly OLR and HRC anomalies to help distinguish between artificial modes of variability and those associated with real variability.

Results from the analysis show that significant errors are introduced by changes in the satellite ECT, and they appear differently in the two datasets. The primary satellite-related bias in the OLR appears as the fourth REOF mode, which accounts for 4.4% of the OLR anomaly variance. Its spatial pattern exhibits a strong surface signature over land, with the opposite sign over many of the deep convective regions of the ocean. During some periods, these biases result in widespread errors of over 10 W m^{-2} , which are sustained for several months to over a year. In other cases, the transition between satellites induces abrupt, artificial changes in the OLR as high as 16 W m^{-2} . In the HRC, the satellite-related bias appears as the leading two REOF modes, which account for 13.1% of the HRC anomaly variance. The spatial patterns of the HRC biases are indicative of an overall change in the mean climatological convection pattern. The above results can be understood by considering the sampling and radiometric characteristics of the OLR and HRC datasets.

To remove the satellite ECT biases, the REOF time series of the satellite-related modes are modified by using the detailed knowledge of the satellite ECTs so that only artificial variability related to the satellite changes is captured and the natural variability is excluded. These modified time series are used in conjunction with their associated spatial patterns to compute the satellite-related artificial variability, which is then removed from the two datasets. These datasets provide an improved resource to study intraseasonal and longer timescale regional climate variations, large-scale interannual variability, and global-scale climate trends. Analyses of the long-term trends in both datasets show that the satellite biases induce artificial trends in the data and that these artificial trends are reduced in the corrected datasets. Further, each of the corrected datasets exhibits a trend in the tropical western-central Pacific that appears spatially independent of the satellite biases and agrees with results of previous studies that indicate an increase in precipitation has occurred in this region over the period encompassed by these datasets.

1. Introduction

In recent years, global climate change and variation have become significant public concerns. To understand the climate system and its variations, long-record datasets are essential for determining and distinguishing natural variability from climate trends. Datasets for such climate studies often consist of in situ observations (e.g., surface observations, upper-air networks, aircraft, ocean

moorings, etc.), satellite measurements, or derived products from one or both of these sources. In situ observations are highly valuable for long-term climate change studies due to the very long records available for particular points (e.g., temperature and sea level records, tree rings, etc.). However, these records are usually subject to extremely inhomogeneous and sparse sampling in space, especially over oceans, and thus may not always be adequate for addressing large-scale climate questions. Satellite measurements and their products, on the other hand, have much better spatial sampling characteristics for the given period of coverage. For this reason, they are widely used for studies of large- to global-scale climate variations on intraseasonal to interannual timescales since many satellite datasets now extend over several years. Such satellite datasets include those for the outgoing longwave radiation (OLR; Gruber and Winston 1978), highly reflective cloud (HRC; Gar-

Current affiliation: Research and Data Systems Corporation, Greenbelt, Maryland.

Corresponding author address: Dr. Duane E. Waliser, Institute for Terrestrial and Planetary Atmospheres, State University of New York at Stony Brook, Stony Brook, NY 11794-5000.
E-mail: waliser@terra.msfc.sunysb.edu

TABLE 1. Satellite information related to the production of the OLR and HRC datasets. (SR is scanning radiometer; AVHRR is Advanced Very High Resolution Radiometer.)

Satellite	Launch date	Operational date	Standby date	Deactivation of end of operations date	Nominal crossing time (LST)	Orbital drift rate (min/month)	Window channel and sensor for OLR
ESAA-9	26 February 1969	*	*	20 November 1972	1543	2.9	*
ITOS-9	23 January 1970	*	*	17 June 1971	1549	3.4	*
NOAA-1	11 December 1970	12 December 1970	*	19 August 1971	1508	2.8	*
NOAA-2	15 October 1972	19 November 1972	19 March 1974				SR series
		1 July 1974	16 October 1974	30 January 1975	0844	−0.5	
NOAA-3	6 November 1973	19 March 1974	1 July 1974				
		16 October 1974	17 December 1974	31 August 1976	0827	−0.6	10.5–12.5 μm
NOAA-4	15 November 1974	17 December 1974	15 September 1976	18 November 1978	0835	−0.4	SR
NOAA-5	29 July 1976	15 September 1976	1 March 1979	16 July 1979	0836	0.9	
TIROS-N	13 October 1978	6 November 1978	*	27 February 1981	1530	**	10.5–11.5 μm
NOAA-6	26 June 1979	16 July 1979	20 June 1983	31 March 1987	0730	**	AVHRR
NOAA-7	23 June 1981	24 August 1981	*	7 June 1986	1430	**	
NOAA-9	12 December 1984	25 February 1985	8 November 1988	22 May 1996	1430	**	11.5–12.5 μm
NOAA-11	24 September 1988	8 November 1988	10 April 1995	*	1430	**	AVHRR
NOAA-12	14 March 1991	17 September 1991	*	*	0730	**	
NOAA-14	30 December 1994	10 April 1995	*	*	1430	**	

* Not available/applicable.

** Exact drift is given in Fig. 2.

cia 1985), microwave sounding unit (Spencer 1993), sea surface temperature (SST; Reynolds 1988), International Satellite Cloud Climatology Project (ISCCP; Rossow and Schiffer 1991), and Earth Radiation Budget Experiment (ERBE; Hartmann et al. 1986; Harrison et al. 1990).

In this study, we are concerned with the Outgoing longwave radiation and highly reflective clouds datasets. These two datasets have time spans of 22 and 17 yr, respectively, and each covers several El Niño–Southern Oscillation (ENSO) events. OLR is an estimate of the total outgoing infrared radiation at the top of the atmosphere inferred from multiband satellite radiation measurements using the method of Gruber and Krueger (1984). OLR has been used to study the ENSO phenomenon (e.g., Gill and Rasmusson 1983; Rasmusson and Wallace 1983; Lau and Chan 1988) and relationships between large-scale characteristics of convection, sea surface temperature, and wind (e.g., Graham and Barnett 1987; Gutzler and Wood 1990; Waliser and Graham 1993); to describe tropical, as well as global, climate trends (Graham 1995); and to investigate convective activity and precipitation in the Tropics (Nitta and Yamada 1989; Morrissey and Graham 1996). HRC is a binary indicator of the presence of organized deep convection in the Tropics derived subjectively from daily (daytime) visible and infrared satellite mosaics (Garcia 1985). The monthly HRC dataset is computed by combining these daily images (i.e., zeros and ones) into maps with units of days per month that deep convection was present. HRC has been used to study ENSO (e.g., Ramage and Hori 1981), to examine the general climatological features of large-scale convection (Zimmerman et al. 1988; Hastenrath 1990; Waliser et al. 1993; Waliser and Gautier 1993), and to diagnose the surface wind field (Zebiak 1990).

While the long-record characteristic of the OLR and HRC datasets makes them an invaluable resource for climate study, their year-to-year accuracy is suspect due to the changes that have occurred during the period of their derivation. Table 1 lists the various satellites used over the years to derive these two datasets, while Fig. 1 shows similar information graphically. This information will be discussed in more detail in the next section. However, it can be seen that several different satellites with different satellite equatorial crossing times (ECTs), and even different sensor characteristics, were used over these years to derive these two datasets. Thus, biases related to satellite and sensor changes may exist in these datasets.

In fact, in their study of large-scale interannual variability of monthly OLR over the global Tropics, Cheliah and Arkin (1992) performed rotated principal component analysis on OLR for the period from 1974 to 1989 and found what appeared to be a “nonphysical” mode (the third mode in their study). They pointed out that the changes in the time series for this mode were closely related to the abrupt changes in the satellite ECTs associated with morning and afternoon satellites. However, no attempt was made to remove these biases.

By comparing the OLR and rainfall in India, Gadgil et al. (1992) deduced that there is a systematic bias in the OLR dataset and pointed out that the bias should be removed before the dataset is used for the study of interannual variations. They found that there are large systematic differences between the mean July–August OLR for the periods 1974–77 [National Oceanic and Atmospheric Administration (NOAA) scanning radiometer (SR) series, i.e., NOAA-2–NOAA-5; morning ECT] and 1982–85 (NOAA-7; afternoon ECT). In designing a scheme to correct the biases, they assumed,

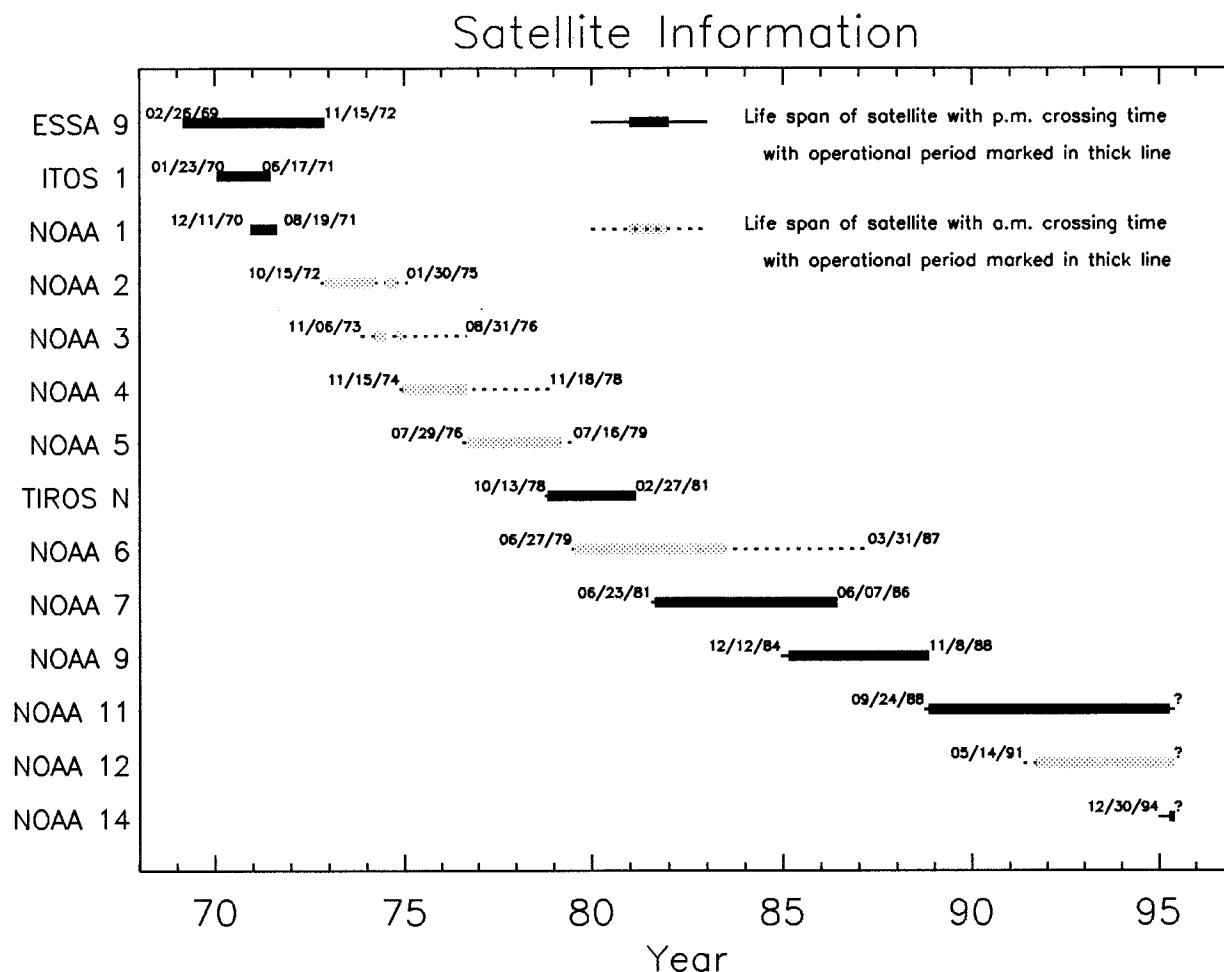


FIG. 1. Satellite information. Dates labeled in the figure are satellite launch (left end) and deactivation–end of operations (right end); question marks (?) denote unknown date.

somewhat arbitrarily, that the distribution of OLR differences between the two periods for each grid should be symmetric about zero. Then OLR from *NOAA-7* was modified through a second-order fitting equation with coefficients to be determined so that the difference of OLR for the two periods would show symmetric distributions about zero. In their scheme, the part of the OLR chosen to be modified is arbitrary (e.g., it could be the NOAA SR series instead of *NOAA-7*). In other words, the correction is not linked explicitly to a specific bias producing cause, and the method may result in an artificial offset to the corrected OLR. Moreover, it would be difficult to apply this method to the full OLR record, which contains satellites with more than just two distinct ECTs.

Kayano et al. (1995) also reported a satellite-related mode in their empirical orthogonal function analysis (EOF) of OLR anomalies. They developed a simple method to remove these biases in the OLR by removing the mean patterns of OLR anomalies for each of the three periods during which *TIROS-N*, *NOAA-6*, and

NOAA-7, *-9*, and *-11* were operational, respectively. However, as they recognized and pointed out, the method would remove real interannual variability as well. Furthermore, the methods of Kayano et al. (1995), as well as that of Gadgil et al. (1992), do not take into account the effects due to the slow drift of satellite ECTs.

While the discussion and studies above focus on the OLR dataset, the HRC dataset is subject to similar biases, given that it is derived mostly from the same set of satellites. The extreme utility of both the OLR and HRC datasets warrants a more comprehensive and complete method to remove the biases from these datasets. In this study, rotated empirical orthogonal function analysis (REOF) is performed on the OLR and HRC datasets. Based on results from this analysis, along with detailed satellite information, the modes related to satellite ECTs, as well as modes that have physical meanings, are identified. The methods are developed to remove the corresponding biases from the datasets. Compared to those of Gadgil et al. (1992) and Kayano et al. (1995), the methods developed in this study are more

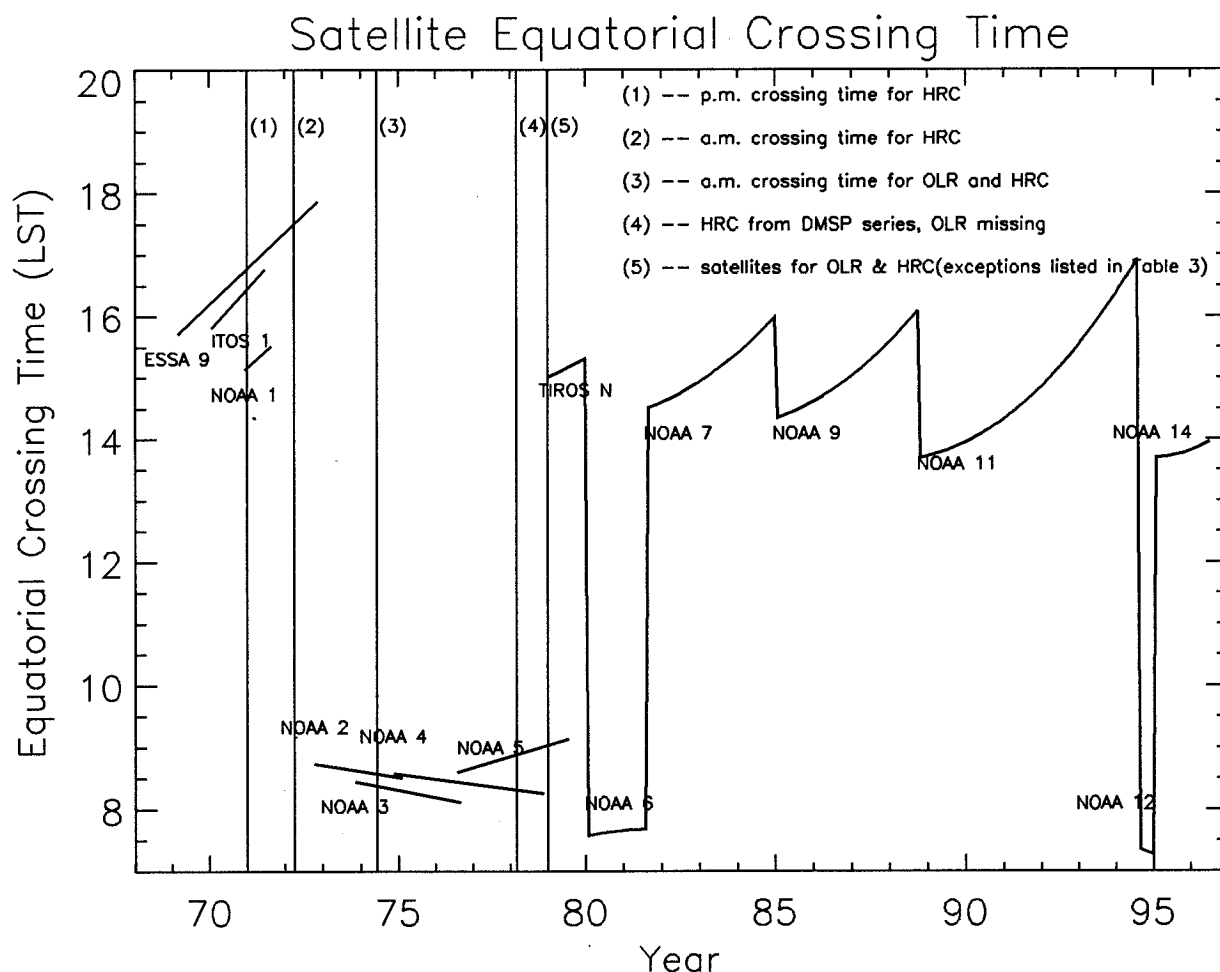


FIG. 2. Satellite equatorial crossing times. Exact satellite crossing times after 1978 are provided by the TeraScan (a product of SeaSpace, San Diego, CA) weather satellite receiving system database, while before 1979 they are only estimates (see text for further details). Numbers within vertical lines denote periods with features listed in the figure.

explicitly linked to the causes of the bias and in addition are more robust. Section 2 provides a detailed description of the datasets and pertinent satellite information. Section 3 discusses the methodology applied in this study. Section 4 identifies and removes the biases from the datasets. Section 5 discusses the differences between the biases in the OLR and HRC datasets and also discusses the overall trends in the datasets before and after the bias removal procedures. Section 6 provides a brief summary of the results.

2. Data and satellite information

a. Satellite information

Since the primary goal of this study is to remove the biases in the OLR and HRC datasets related to satellite ECTs, it is essential to know these ECTs, along with any other relevant sensor or methodology information, for all the satellites used to derive the OLR and HRC datasets. Table 1 lists this information for all the relevant

satellites. These satellites are sun-synchronous and polar orbiting, and thus in the Tropics provide only two passes per day, 12 h apart. Only the daytime ECTs are listed in Table 1. Satellite standby dates are also listed. A satellite on standby only transmits sensor health and housekeeping information, and thus is not used in the derivation of the OLR and HRC datasets. The satellite ECTs listed in Table 1 are not exact due to the orbital drift of each satellite and are thus referred to as the nominal ECTs. The nominal ECT is listed in various sources (Johnson et al. 1976; Gruber and Krueger 1984; Gruber and Chen 1988; Chelliah and Arkin 1992; L. Ranne 1996, personal communication). Figure 2 shows the drift of the ECT for each satellite. After 1978, the ECT is based on information in the orbital element database of the TeraScan¹ weather satellite receiving system. Before 1979, the drift rate of the ECT for each

¹ TeraScan is a product of SeaSpace, of San Diego, California.

TABLE 2. Timetable of the satellites and their equatorial crossing times used to produce the OLR dataset.

Data period	Satellite(s)	Crossing time (LST)
June 1974–February 1978	NOAA-2–NOAA-5	A.M.
March 1978–December 1978	Missing data	
January 1979–January 1980	TIROS-N	P.M.
February 1980–August 1981	NOAA-6	A.M.
September 1981–February 1985 ^a	NOAA-7	P.M.
March 1985–November 1988 ^b	NOAA-9	P.M.
December 1988–August 1994	NOAA-11	P.M.
September 1994 ^c –December 1994	NOAA-12	A.M.
January 1995–July 1996	NOAA-14	P.M.

^a Monthly mean for February 1985 is a mixture of NOAA-7 and NOAA-9.

^b Monthly mean for November 1988 is a mixture of NOAA-9 and NOAA-11.

^c Monthly mean for September 1994 is a mixture of NOAA-11 and NOAA-12.

satellite was taken from Johnson et al. (1976). This linear drift rate is used in Fig. 2, along with the assumption that the nominal ECT is the ECT at launch.

From Table 1 and Fig. 1, we can see that there are periods during which more than one satellite is operational. For example, NOAA-6, a satellite with a morning ECT, was operational starting 16 July 1979 and was on standby starting 20 June 1983. However, NOAA-7, a satellite with an afternoon ECT, was operational starting 24 August 1981, which is before the time that NOAA-6 was put on standby. For these overlapping periods, Table 1 does not provide enough information to determine which satellite was used to derive the OLR or HRC dataset. Fortunately, the derivation of the OLR dataset for most periods has been well documented in many sources (Gruber and Krueger 1984; Gruber and Chen 1988; Chelliah and Arkin 1992; Kayano et al. 1995; J. Janowiak 1996, personal communication). Based on these sources, Table 2 lists each period and the corresponding satellite(s) used to derive the OLR. The only undocumented period is from June 1974 to February 1978, when NOAA SR series (NOAA-2–NOAA-5) was operational. However, these satellites share essentially the same ECT, sensor, and water vapor window channel, and thus for the purposes of this study are viewed as if they represent the same satellite.

Unfortunately, information on the derivation of the HRC dataset is much less clear. The only information source is the HRC atlas (Garcia 1985), which has been found to contain some inaccuracies. For example, the atlas lists *ITOS-1*, *ESSA-9*, and *NOAA-1* as the sources for the HRC data during the period from January 1971 to May 1974 and indicates that they have morning ECTs. However, we can see from Table 1 (or Fig. 1, or Rao et al. 1990) that these satellites all have afternoon ECTs. Also, the latest date of the end of operations of these three satellites is 20 November 1972, with the longest-lasting satellite being *ESSA-9*. This means that during

the period from November 1972 to May 1974, the HRC could not have been derived from these three satellites. Instead, we find that only NOAA-2 and NOAA-3 were operational during this period. While such uncertainties make it harder for us to remove the satellite-related bias in the HRC dataset, significant effort has been undertaken in this study to minimize their influence. First, information in Table 1 and Fig. 1 are used to identify periods when there was only one operational satellite. For these periods, it is possible to determine with greater certainty whether the HRC was derived from a morning or afternoon satellite for the period. Then, for periods with more than one operational satellite, which fortunately are few and relatively short (a few months each), the satellites used for HRC derivation are determined from a combination of the available documentation and results of the rotated empirical orthogonal function analysis. This procedure will be discussed in more detail below; however, the results pertaining to the estimated satellite timetable of the HRC derivation are listed in Table 3, along with changes from the documentation given in Garcia (1985).

b. OLR

NOAA SR series satellites used the scanning radiometer, while *TIROS-N* and NOAA-6, -7, -9, -11, -12, and -14 used the Advanced Very High Resolution Radiometer (AVHRR) to estimate OLR (Table 1). The window channels chosen to estimate OLR are also listed. OLR flux estimates were derived by using theoretical infrared radiative transfer models to convert the narrowband radiance measurements from the chosen window channel to broadband OLR fluxes (Gruber and Krueger 1984). The OLR dataset that is available from NOAA has had some corrections applied for the various changes in instruments and spectral windows (Gruber and Krueger 1984), but not for changes in local measurement times among different NOAA satellites. Table 1 lists the various NOAA satellites, along with their nominal ECTs, applicable window channels, and operational period. Figure 2 shows the known drift of the ECT. As mentioned earlier, prior to 1979, the drifts shown in Fig. 2 are estimated values.

The OLR dataset used in this study is for monthly mean OLR on a $2.5^\circ \text{ lat} \times 2.5^\circ \text{ long}$ grid. The dataset is 266 months long, from June 1974 to July 1996, with a 10-month gap from March 1978 to December 1978, and covers the domain 30°S to 30°N . The annual cycle of the OLR is computed based on the whole dataset, and then the OLR anomalies are computed with respect to the annual cycle. In the following sections, if not explicitly specified, OLR refers to the OLR anomalies.

c. HRC

Garcia (1985) developed a subjective method for using both visible and infrared satellite mosaics (infrared

TABLE 3. Timetable of the satellites and their equatorial crossing times used to produce the HRC dataset, along with remarks concerning the determination of whether the given period–satellite was considered to have a morning or afternoon satellite ECT.

Data period	Crossing time	Satellite(s)	Remarks
January 1971–March 1972	P.M.	<i>ITOS-1</i> , <i>ESSA-9</i> , <i>NOAA-1</i> ^a	From Garcia (1985)
April 1972–October 1972	A.M.	<i>ESSA-9</i> ^a	Garcia (1985) specifies P.M. However, during the last 7 months of <i>ESSA-9</i> , the data exhibit features more similar to A.M. satellites consistent with the drift seen in Fig. 2.
November 1972–May 1974	A.M.	<i>NOAA-2</i> – <i>NOAA-3</i> ^a	Garcia (1985) specifies <i>ITOS-1</i> , <i>ESSA-9</i> , and <i>NOAA-1</i> . However, this period occurs after the lifetime of these satellites.
June 1974–February 1978	A.M.	<i>NOAA-2</i> – <i>NOAA-5</i>	From Garcia (1985)
March 1978–December 1978	A.M.	DMSP ^b series (<i>F-1</i> , <i>F-2</i> , <i>F-3</i>)	<i>F-1</i> : P.M. crossing time; <i>F-2</i> , <i>F-3</i> : A.M. crossing time. No information on which satellite was actually used; set to A.M.
January 1979–June 1979	P.M.	<i>TIROS-N</i>	From Garcia (1985)
July 1979–August 1979	A.M.	<i>NOAA-6</i>	Garcia (1985) specifies <i>TIROS-N</i> ^c
September 1979–January 1980	P.M.	<i>TIROS-N</i>	From Garcia (1985)
February 1980–August 1981	A.M.	<i>NOAA-6</i>	From Garcia (1985)
September 1981–January 1982	A.M.	<i>NOAA-6</i>	Garcia (1985) specifies <i>NOAA-7</i> ^c
February 1982–May 1982	P.M.	<i>NOAA-7</i>	From Garcia (1985)
June 1982–September 1982	A.M.	<i>NOAA-6</i>	Garcia (1985) specifies <i>NOAA-7</i> ^c
October 1982–February 1985	P.M.	<i>NOAA-7</i>	From Garcia (1985)
March 1985–December 1987	P.M.	<i>NOAA-9</i>	From Garcia (1985)

^a Infrared not used until 1974.

^b DMSP: Defense Meteorological Satellite Program.

^c Both satellites indicated were operational, O. Garcia notes (1996, personal communication) that either satellite may have actually provided the data for the HRC. Better agreement was found using the satellite indicated; see section 4d.

mosaics were not used until June 1974) to create daily, binary indicators of tropical large-scale deep convection. In creating this dataset, called the highly reflective clouds, daytime infrared information was used as a proxy for cloud-top height so as to filter out low- and midlevel clouds, and thus to indicate the presence of high-level convective cloud systems. The daytime visible satellite mosaics are used to exclude the large-scale thin cirrus clouds associated with convective systems. The resulting HRC dataset is thus composed of once-per-day maps of ones and zeros with 1° lat \times 1° long spatial resolution, where ones identify regions of deep convection. The monthly HRC data (i.e., frequency counts) are formed from these daytime images and thus have units of days per month (of deep convection present at each grid point).

The HRC data used in this study are the monthly values on a $2^\circ \times 2^\circ$ grid. The dataset is 204 months long, from January 1971 to December 1987, and covers 25°S to 25°N . The annual cycle of the HRC is computed based on the whole dataset, and the HRC anomalies are computed with respect to the annual cycle. In the following sections, if not explicitly specified, HRC refers to the HRC anomalies.

3. Methodology

One frequently used technique for studying interannual and low-frequency climate variability is empirical orthogonal function analysis. This technique is adopted in this study to identify the most common modes of

variability in the tropical OLR and HRC datasets, as well as to pinpoint the modes that are related to satellite ECTs (hereafter referred as satellite modes). Unrotated empirical orthogonal function analysis maximizes for each mode (i.e., often referred to as an eigenvector, eigen function, or principal component) the variance explained over the entire analysis domain, subject to the requirement that the modes have strict spatial and temporal orthogonality. Due to the criterion that the first mode must contain the maximum variance possible, the second mode the maximum of the remaining variance, and so on, the resulting EOF modes are sensitive to the analysis domain and the spatial resolution of the data. These latter features make unrotated EOF analysis less accurate in portraying the physical relationship embedded within the data (Richman 1986; Chelliah and Arkin 1992). Rotated EOF analysis, on the other hand, can greatly alleviate the above problems. REOF analysis tends to yield more intuitively or physically meaningful results in space and time (Horel 1981), while resolving the same total variance as the unrotated analysis. Richman and Lamb (1985) discuss in detail, with illustrations, the advantages of rotated over unrotated eigenmode analysis. Richman (1986) reviews the features of unrotated and rotated principal components and demonstrates that the rotated principal components are also less subject to sampling errors than the unrotated components.

In this study, unrotated EOF analysis is first performed on both the OLR and HRC anomalies. Rotated

EOF analysis, which was the type of analysis that allowed Chelliah and Arkin (1992) to identify an OLR satellite mode, is then performed using only the EOF modes judged to be significant at the 99% level. This turns out to be the first seven EOF modes for the OLR and the first eight modes for the HRC. A description of the significance test and its results are given in the appendix. Aside from the results of this test, the REOF analysis is highly stable: choosing cutoff numbers between 6 and 15 only causes minor changes in the first few eigenmodes, and the satellite modes are nearly identical in each case. Furthermore, the first few modes are highly insensitive to a wide variety of rotations (e.g., orthogonal quartimax and varimax, or oblique promax and Harris–Kaiser). The rotations shown here were produced from an orthogonal quartimax rotation.² This procedure derives an orthonormal transformation matrix that minimizes the function

$$\sum_j^M \sum_i^P b_{ji}^4,$$

where M is the number of retained modes, P is the number of spatial points, and b is the eigenvector loadings. This transformation matrix multiplies the matrix of unrotated EOF loadings, yielding the matrix of rotated EOF loadings [i.e., the rotated vectors, which tend to have a “simpler structure”; Richman (1986)]. A demonstration of the advantage of using REOF over EOF in this study will be shown in the next section.

4. Analysis and results

a. OLR mode identification

To remove biases from the datasets, we must first know where the biases come from and assess how large they are. To analyze the OLR dataset, REOF analysis is performed and then each eigenmode is examined to determine whether it is geophysically based or related to the satellite biases discussed in section 2 (e.g., ECT bias). While the cutoff number for the EOF rotation is seven EOF modes (see section 3), only the six leading rotated eigenmodes are shown and discussed. Figure 3 shows the spatial loading patterns and associated time series of the OLR REOFs. The spatial patterns are smoothed with a $3^\circ \times 3^\circ$ grid box before contouring. Regions with negative loadings are stippled in the spatial patterns.

The first mode (Fig. 3a) accounts for 9.3% of the anomaly variance. Its spatial loading shows a strong, large-scale, east–west dipole near the equator, with a negative center near 5°N , 130°E and a positive center near 5°S , 170°W . Its associated time series clearly shows all the major El Niño (warm) and La Niña (cold) events

of the equatorial Pacific, such as the La Niña events of 1975–76 and 1988–89, and the El Niño events of 1982–83, 1987, and 1992. For comparison, the smoothed time–longitude variation of meridionally averaged SST anomalies from 5°S to 5°N is shown in Fig. 4; regions with negative SST anomalies are stippled. This canonical ENSO mode, which is essentially the same as the first mode in Chelliah and Arkin (1992), represents the convection anomaly associated with an anomalous Walker circulation with rising (sinking) motion over the eastern Indian Ocean, the Maritime Continent, and the equatorial western Pacific, and sinking (rising) motion over the central and eastern equatorial Pacific during a tropical cold (warm) ENSO event. These canonical ENSO features are consistent with the results of Ropelewski and Halpert (1987, 1989) who studied the global precipitation patterns associated with the low- (El Niño) and high- (La Niña) index phases of the Southern Oscillation index.

The second mode (Fig. 3b), which accounts for 6.8% of the anomaly variance, has a very similar spatial loading pattern to the first mode except for a relative sign change over many of the regions outside the two centers of high loading in the equatorial Pacific. One can see from Fig. 4 that the global–equatorial SST pattern appears to be dissimilar among the different El Niño and La Niña events. For example, the 1972–73 and 1986–87 El Niño events are marked by warming at nearly all longitudes, while the El Niños during 1977–78, 1982–83, and 1992 show weak cooling in the Indian and Atlantic Oceans. A similar observation can be made for the La Niña events occurring in the record. Therefore, this mode appears to account for much of the ENSO variability that is not common to the canonical pattern (i.e., Fig. 3a).

The 1982–83 El Niño was unique in two ways: it was the most dramatic among all the El Niños recorded by this dataset, and it appeared to initiate in the western Pacific rather than in the eastern Pacific, as do most other El Niños (Philander 1991). The features of this El Niño that are common to most other El Niños are captured by a negative peak in the first mode time series and to a lesser extent by a positive peak in the second mode time series. However, those features that are especially unique to the 1982–83 event are dominant characteristics of the third eigenmode (Fig. 3c), which accounts for 5.3% of the anomaly variance. The main feature of the associated time series is a very large negative peak around the time the warm event occurred (December 1982 to February 1983). The spatial loading shows an eastward shift of the anomalous convective centers to the eastern equatorial Pacific relative to the first (canonical ENSO) mode. The positive center is shifted to about 5°S , 140°W , and the negative center is at about 5°N , 160°E . Following Chelliah and Arkin (1992), this mode is referred to as “1982–83 mode” due to its significant relation to the 1982–83 El Niño.

The fourth mode (Fig. 3d; see Fig. 5a), which ac-

² International Mathematical and Statistical Library routine DFROTA.

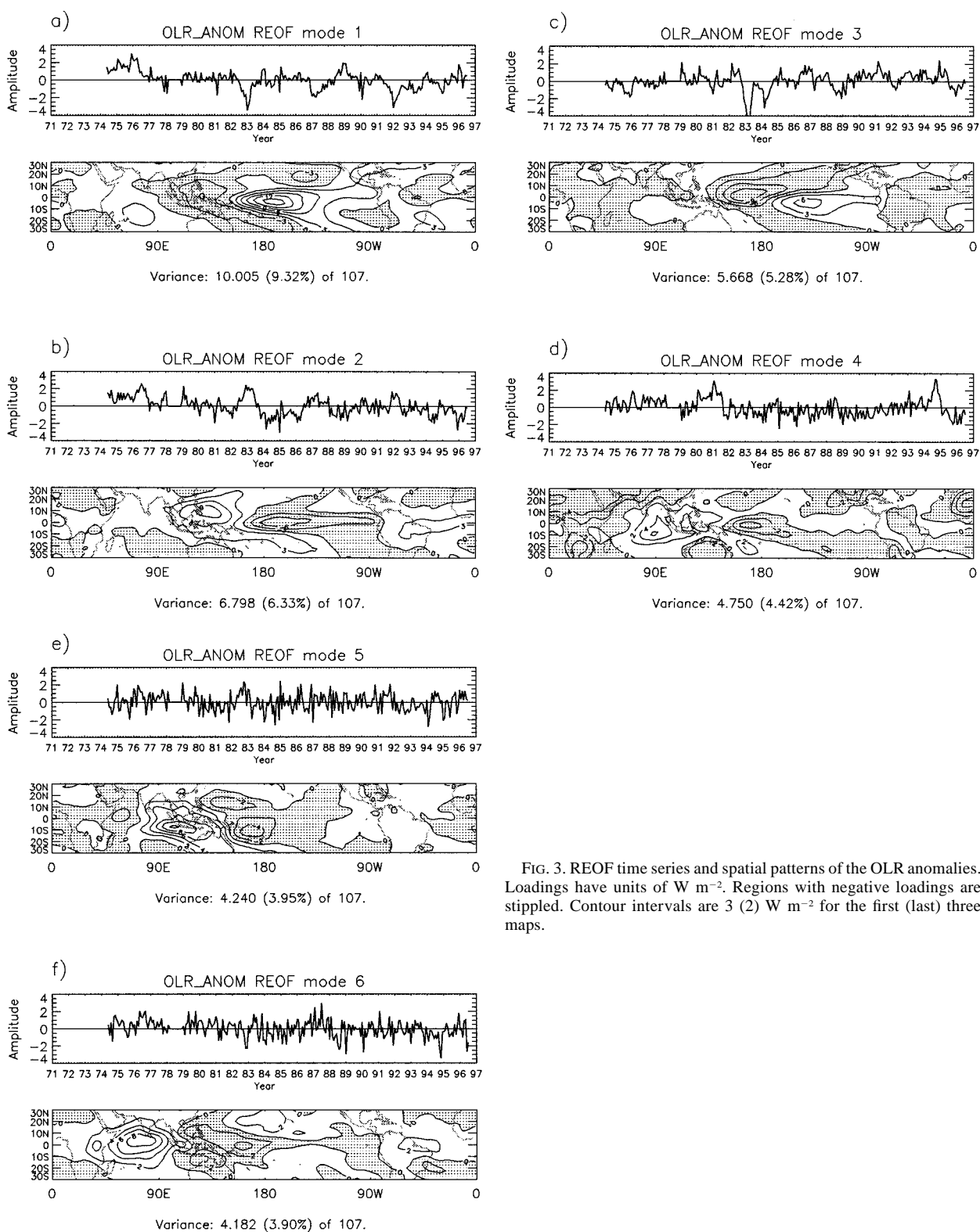


FIG. 3. REOF time series and spatial patterns of the OLR anomalies. Loadings have units of W m^{-2} . Regions with negative loadings are stippled. Contour intervals are 3 (2) W m^{-2} for the first (last) three maps.

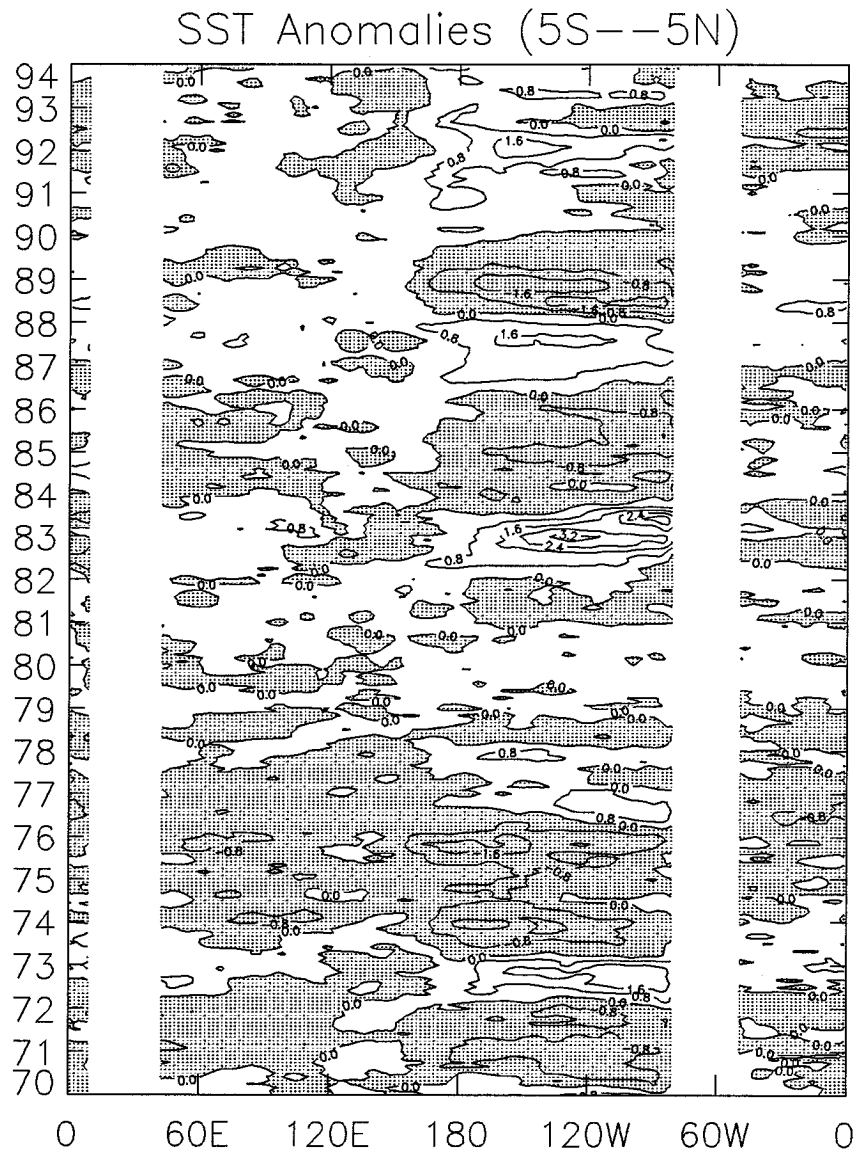


FIG. 4. Time-longitude map of average SST anomalies from 5°S to 5°N. Regions with negative SST anomalies are stippled. Contour interval is 0.8°C.

counts for 4.4% of the anomaly variance, is similar to mode 3 in Chelliah and Arkin (1992; see their Fig. 1). It has negative spatial loading over most of the landmasses in the Tropics and the central equatorial Pacific near the date line, and positive loading over most of the Indian Ocean and some part of the western Pacific. Its time series shows a strong association with changes in the satellite ECTs (Fig. 2). For example, during the period from February 1980 to August 1981 when NOAA-6 (morning ECT) was used to derive OLR (Table 2), the time series amplitude of this mode oscillates near 2.0, while it oscillates near -0.5 for the period from September 1981 to August 1994, when NOAA-7, -9, and -11 (afternoon ECTs) were used to derive OLR. Over the region of the Sahara Desert, the spatial loading value

is about 5 W m^{-2} ; thus, the OLR difference associated with this mode for these two periods is about 12 W m^{-2} . The reasons for this bias will be described below.

The fifth and sixth modes (Figs. 3e and 3f), which account for 4.0% and 3.9% of the anomaly variance, respectively, each exhibit an east-west dipole feature in the vicinity of the tropical Indian and western Pacific Oceans. Their maxima-minima are offset relative to each other by about 30° in longitude, which represents about a 90° phase shift between the two dipoles. The spatial structures of these two modes, along with the (relatively) high-frequency fluctuations evident in their time series, suggest that these two modes represent the eastward-propagating intraseasonal variations in OLR associated with the Madden-Julian oscillation (Madden

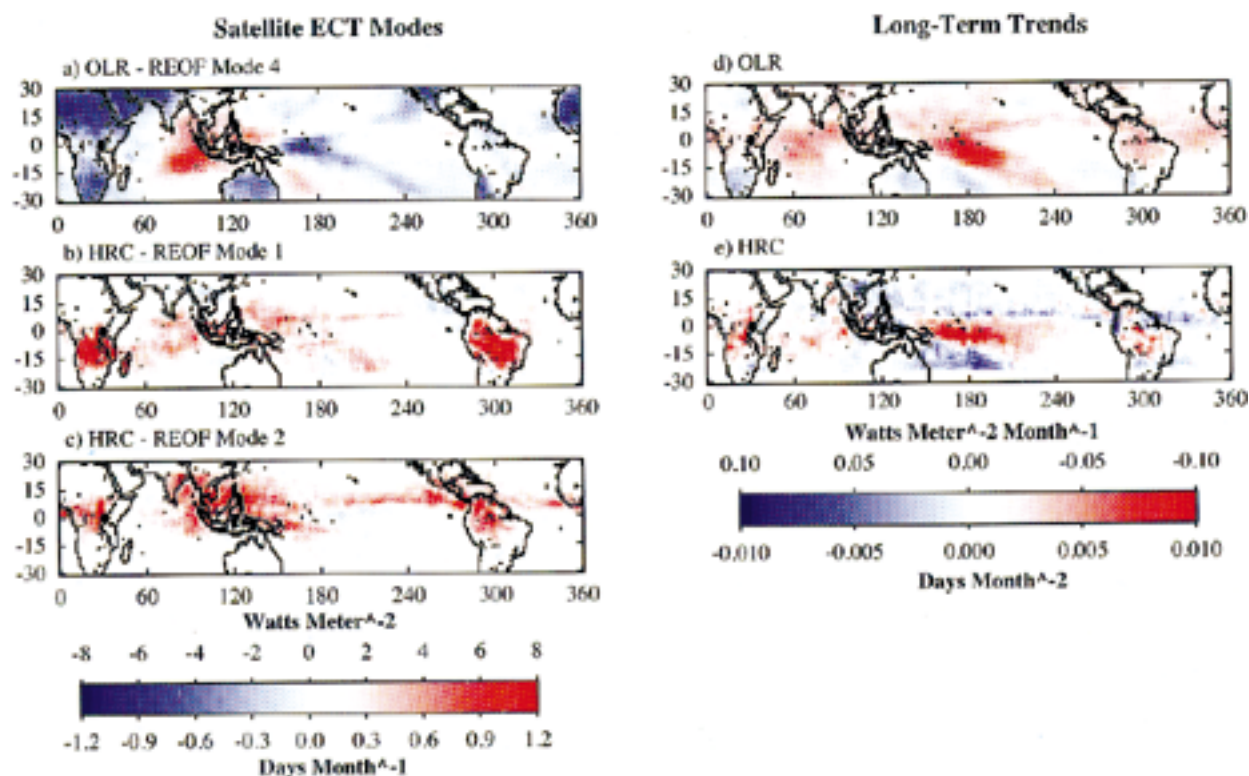


FIG. 5. Satellite equatorial crossing time modes: (a) OLR REOF mode 3, same as Fig. 3d; (b) and (c) HRC REOF modes 1 and 2, same as Figs. 9a,b. Linear trends in the (d) OLR and (e) HRC after the ECT bias-removing procedures have been applied, same as Figs. 12c,d.

and Julian 1972). Evidence for this assertion comes from the nearly identical patterns produced by the EOF analyses of intraseasonally bandpassed OLR of Murakami et al. (1986) and Lau and Chan (1988). In the former (latter), a filter with half-power points at 30–60 and (20–70) days was applied. In both cases, the first two modes of their EOF decompositions are nearly identical to those shown in Figs. 3e and 3f.

It should not be a surprise that the eigenmodes in this study are not exactly the same as in Chelliah and Arkin (1992) and Kayano et al. (1995), given the differences between the input datasets. Chelliah and Arkin (1992) used only 15 yr of OLR data from June 1974 to December 1987 on a $5^\circ \text{ lat} \times 10^\circ \text{ long}$ grid over the domain 30°S to 30°N , with the OLR anomalies computed from a climatology based on the 10-yr period from 1979 to 1988. Kayano et al. (1995), on the other hand, used OLR data for the period from January 1979 to December 1988 over the domain 40°S to 40°N on a $2.5^\circ \times 2.5^\circ$ grid, with the anomalies computed from the same 10-yr

(1979 to 1988) climatology as in Chelliah and Arkin (1992). Kayano et al. also applied a low-pass filter on the OLR anomalies before their EOF analysis.

To demonstrate that the variability associated with the fourth mode is of a significantly artificial nature, both a statistical illustration and a physical example will be given. The statistical illustration is given in Table 4, which shows the correlations between the ECT time series (for the period when the exact ECT was available) and the amplitude time series from each of the modes in the REOF and unrotated EOF analyses. These correlations demonstrate how the rotation procedure was able to isolate ECT variability that was associated with several modes in the unrotated analysis (i.e., the third and sixth modes, and to a lesser extent the second and fifth modes) into a single mode in the rotated analysis (fourth mode). Second, the high value for the correlation strongly suggests that much of the variability associated with the fourth mode is related to ECT changes.

The physical example is embodied in the relation be-

TABLE 4. Correlations between the satellite equatorial crossing time and the time series for each OLR EOF and REOF mode for the period when the exact crossing time is known (i.e., after 1978, $N = 211$ months; see section 2). Correlations greater than 0.3 are in bold.

Mode	1	2	3	4	5	6	7
EOF correlation	-0.18	0.21	0.32	0.19	-0.27	0.57	0.02
REOF correlation	-0.04	0.00	0.03	0.72	-0.17	-0.02	-0.08

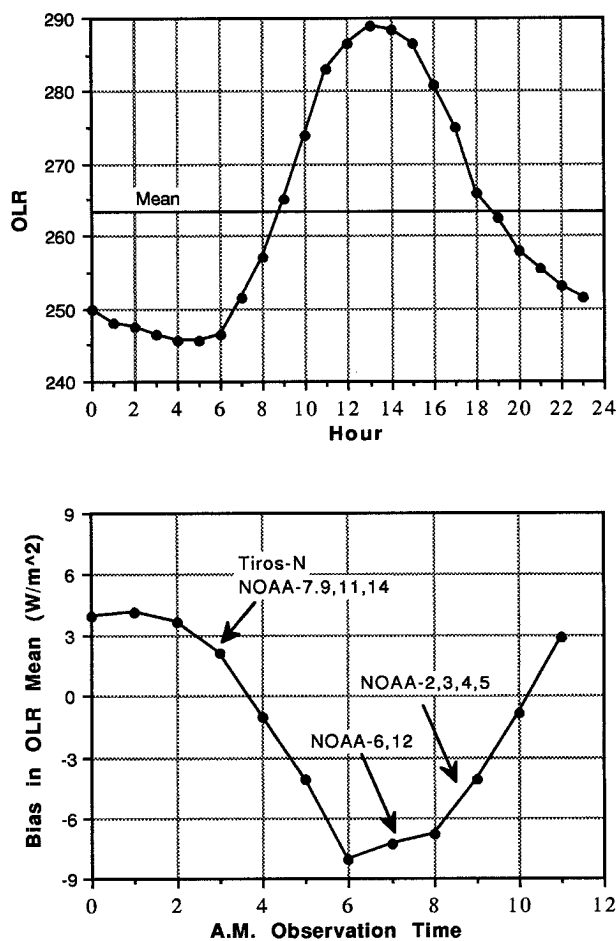


FIG. 6. (top) Mean diurnal cycle of OLR over the Sahara constructed by Kondragunta and Gruber (1995) from three ERBE satellites during their overlap period, 12 June 1986 to 19 January 1997; thin horizontal line denotes the mean. (bottom) Bias in estimating the mean from the top figure when using only two observations separated by 12 h.

tween the fourth REOF mode and the plots in Fig. 6. The top plot shows the diurnal cycle of OLR over the Sahara Desert taken from Kondragunta and Gruber (1995), which was constructed using data from three ERBE satellites during a 45-day overlap period from 6 December 1986 to 19 January 1987.³ The horizontal line gives the “true” mean of this (near-hourly resolved) 24-h diurnal cycle. The bottom plot shows the difference between the daily mean obtained by sampling the diurnal cycle only twice, 12 h apart, and the true mean

³ Of the four locations shown Kondragunta and Gruber’s report (the Sahara, the southeast Pacific, the southeast Atlantic, and the central Andes), only the Sahara was chosen for comparison since the climate there tends to be the most stationary of the four locations with respect to synoptic, seasonal, and interannual variations. Such variations render the 45-day (El Niño year) composites of the other locations relatively meaningless for the present purpose.

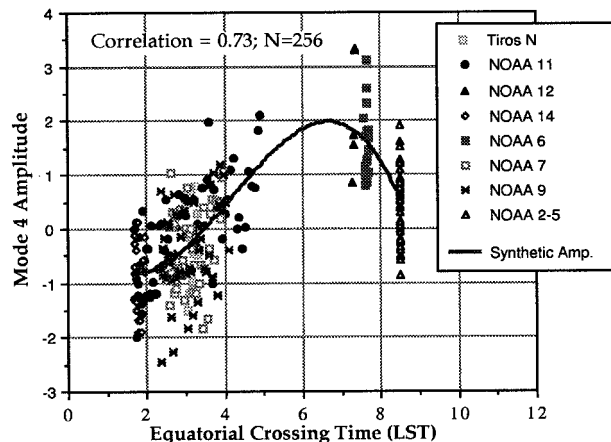


FIG. 7. Scatterplot of the satellite ECTs and the amplitude time series from the fourth OLR REOF mode. Solid line shows the order-three polynomial best-fit regression of the data.

in the top plot. As illustrated in the plot, the (two sample) diurnal mean obtained using NOAA-6 observation times will be about $\sim 7.5 \text{ W m}^{-2}$ lower than the true mean and the (two sample) diurnal mean obtained using NOAA-7 will be about $\sim 2.0 \text{ W m}^{-2}$ higher, representing about a 9.5 W m^{-2} difference between the mean Sahara OLR observed by these the two satellites. This is reasonably consistent with the magnitude of the mode 4 changes occurring over the Sahara between the NOAA-6 and NOAA-7 time periods, given the short time period for deriving the composite diurnal cycle. Similar results hold for differences between NOAA-2 and NOAA-7.

While the above discussion is only representative of one location, some additional confidence regarding the spatial structure of the ECT mode is afforded by the diurnal variations in ISCCP total cloudiness described by Kondragunta and Gruber (1994). The spatial patterns of their first two EOF modes of mean January diurnal variations imply a strong systematic change in the nature of the diurnal cycle in cloudiness between the positive and negative regions of Fig. 3d. Unfortunately, little more can be garnered from their results since the question involves knowing, in addition to the diurnal cycle of cloudiness, how this cycle translates into the diurnal cycle of local OLR and then, even more complex, how the twice per day (12 h) satellite sampling of this cycle ends up producing a bias from the long-term mean (e.g., Fig. 6, bottom).

While the above discussion is meant to illustrate that a large portion of the variability of the fourth OLR REOF mode can be attributed to satellite ECT changes (i.e., abrupt jumps and longer-term trends), some portion of the variability is associated with natural variability that from month to month has a nonzero projection onto this mode’s spatial pattern. It is important that to the extent possible, only the ECT-related variability be removed from the dataset. Figure 7 shows the scatterplot of the amplitudes of the fourth mode (time series in Fig.

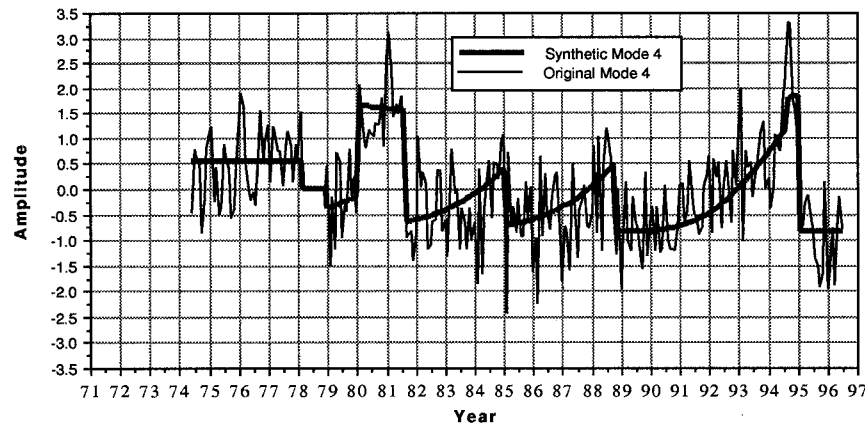


FIG. 8. Estimate of true artificial ECT variability (thick line) associated with the fourth OLR REOF mode based on the regression shown in Fig. 7. The black line is the actual amplitude time series from the fourth mode (i.e., Fig. 3d).

3d) and the associated ECT values. Note, in absence of exact times, that the ECT values before 1979 were approximated as 0800 LST using the data in Table 1. The relationship in Fig. 7 is similar to that shown in Fig. 6 (bottom), each having an inflection point around 0600 LST. The sign is different due to the fact that the value in Fig. 7 has to be weighted by the spatial pattern, which is negative over the Sahara. Once this weighting is taken into account, the two show good agreement over the Sahara. As would be the case when removing the satellite sampling bias for the Sahara alone (e.g., Fig. 6, bottom), it is necessary to remove the “global” dependency of the error–bias on the local observing time, represented here by the scatterplot in Fig. 7 and the associated spatial pattern in Fig. 3d. The order three polynomial regression shown in Fig. 7 is a “best guess” at this dependency ($y = 0.42 - 1.61x + 0.59x^2 - 0.047x^3$, where x is the A.M. ECT).

Figure 8 shows an “interpolated” amplitude (thick line) using the regression relation from Fig. 7. In order to produce an estimate of the biases–errors introduced into the tropical OLR monthly dataset, the spatial pattern of the fourth REOF mode (Fig. 3d) is multiplied by the synthetic time series shown in Fig. 8 to obtain the part of the anomaly variance that is believed to be only due

to ECT changes. By using this interpolated curve and not the actual amplitudes of the fourth mode (i.e., thin line), we expect to leave natural variability, which may from month to month have a nonzero projection onto this mode’s spatial pattern. This type of natural variability accounts for the “noise” about the best guess or interpolated value (thick line).

b. OLR bias removal

To remove the artificial variability due to ECT changes, the synthesized ECT mode described above is subtracted from the OLR anomaly dataset. This reduces the total anomaly variance from 107 to 105 (W m^{-2})². REOF analysis is performed on the new bias-removed OLR anomalies to determine the degree to which the bias-removal procedure has been effective at removing the unwanted variability. To avoid redundancy, the spatial patterns are not shown; however, Table 5 shows the linear correlations between the time series amplitudes of the REOF modes before and after the bias-removal procedure. The table demonstrates that all (i.e., the first seven) of the physical modes of the original dataset (i.e., modes other than mode 4) are well captured by one or a combination of two modes in the bias-corrected dataset (indicated in boldface). For example, the canonical ENSO mode still shows up as mode 1, the second and third modes before the bias removal show up as the third (and to a lesser extent the sixth) and second modes after the bias removal, the fifth and sixth modes before the bias removal show up as the fifth and (primarily) the fourth modes after the bias removal, etc. Further, all the modes in the new bias-corrected dataset have very poor correlation with the original mode 4 (the greatest is -0.23). The results in this table illustrate that the above methodology is an effective approach for removing the unwanted–artificial ECT variability in the tropical OLR data.

TABLE 5. Correlation of OLR REOF time series before and after bias removal. Correlations greater than 0.3 are in bold.

Mode no.	Before						
	1	2	3	4	5	6	7
After							
1	0.94	−0.32	0.07	−0.04	−0.01	0.04	−0.02
2	−0.04	0.09	0.99	0.04	−0.03	0.01	−0.05
3	−0.24	−0.73	0.05	−0.16	−0.07	0.14	−0.17
4	−0.06	−0.08	−0.01	0.16	0.12	0.93	0.08
5	0.04	0.03	0.03	0.04	0.97	−0.08	0.01
6	0.21	0.59	−0.06	−0.23	−0.11	0.32	−0.17
7	−0.02	0.03	−0.06	0.06	0.06	0.00	−0.97

c. HRC mode identification

Figure 9 shows the rotated EOF eigenmodes of the HRC anomalies. As with the OLR, only the first six rotated modes are presented and discussed, even though the actual rotation included eight modes (see section 3). The first mode (Fig. 8a; see Fig. 5b), which accounts for 6.6% of the anomaly variance, has positive spatial loading over most of the Tropics, with two strong centers near 10°S over the landmasses of southern Africa and South America, and a weak center near the equator around the Maritime Continent. The second mode (Fig. 9b; see also Fig. 5c), which accounts for 6.5% of the anomaly variance, has positive spatial loading over most of the domain, with centers around 5°N over Africa, the Maritime Continent, and South America. Even though the annual cycle has been removed, both of the two modes exhibit some similarity to the long-term overall mean HRC distribution (Fig. 10), except for a meridional shift and a relative enhancement over land. The associated time series of these two modes both show cyclic behavior with an annual time period. However, these annual-scale oscillations fluctuate around different values for different periods. For example, in mode 1 (Fig. 9a), the oscillations fluctuate around a negative value during the period from 1973 to 1978 but fluctuate around a positive value during the period from 1983 to 1987. Moreover, oscillations that fluctuate around negative values all have similar amplitudes, as do those that fluctuate around positive values, implying that these oscillations can be roughly categorized into two groups according to the mean values they fluctuate around. By examining these two time series and the information in Table 1 and Fig. 2, we find that the two groups of oscillations for both modes are closely correlated with changes in the satellites, especially changes in the satellite ECT (morning or afternoon). In fact, based on these apparent biases, the 12-month annual cycles computed from morning viewing satellites will not be the same as that computed from the afternoon viewing satellites. This implies that the annual cycle computed from the whole data period will be a weighted mean of the two annual cycles computed from the morning and afternoon views. Thus, removing this long-term mean annual cycle will still leave annual-scale residual oscillations in the data, with the oscillations being different for the morning and afternoon satellite periods. For example, assuming that an afternoon view of the annual cycle of deep convection will have a larger amplitude than a morning view of the annual cycle,⁴ the two annual cycles can be expressed as

afternoon view

$$y_a = (a + \delta)[1 - \sin(2\pi x/12)] \quad (1)$$

and

morning view

$$y_m = (a - \delta)[1 - \sin(2\pi x/12)], \quad (2)$$

where x is the month from 1 to 12. Further, if we assume that the periods containing satellites with morning and afternoon ECT are of the same length (which is nearly the case for the HRC data), then the mean annual cycle of the whole data period is the average of the above cycles:

mean annual cycle

$$y = (y_a + y_m)/2 = a[1 - \sin(2\pi x/12)]. \quad (3)$$

If we remove this mean annual cycle (y), the residuals for periods with afternoon and morning ECT will be

afternoon view

$$y' = y_a - y = +\delta[1 - \sin(2\pi x/12)] \quad (4)$$

and

morning view

$$y' = y_m - y = -\delta[1 - \sin(2\pi x/12)], \quad (5)$$

respectively. The residuals still have annual-scale oscillations and will exist in the HRC anomalies.

The reason for the larger loadings over land in these two modes is also related to the satellite ECTs. Diurnal variations in convection are generally larger over land than over ocean (e.g., Hendon and Woodberry 1993), so that biases introduced by changes between afternoon and morning satellite ECTs will be stronger over land than over ocean. Indeed, the first two modes shown in Fig. 9 tend to produce enhanced positive HRC anomalies, especially over land, when the satellite ECT is in the afternoon. The above discussion strongly suggests that these two modes represent satellite-related biases in the HRC dataset.

The third mode (Fig. 9c), which accounts for 4.4% of the anomaly variance, is the canonical ENSO mode of the HRC, with features similar to the first OLR mode (Fig. 3a). Because of the way the raw HRC data are produced (binary values of “deep convection” sampled once per day), it is not surprising that the HRC spatial loading is not as smooth as that of OLR (cf. Waliser et al. 1993). The time series of this mode consists mainly of interannual variability with strong signals during the 1972–73, 1976–77, and 1987 El Niño events.

The fourth mode (Fig. 9d), which accounts for 4.3% of the anomaly variance, is dominated by the 1982–83 El Niño event. The time series and spatial loading over the Pacific basin are remarkably similar to the 1982–83 mode of the OLR (Fig. 3c). However, there is a relative change between the OLR and HRC patterns in the signs of the loadings over most of the African and South

⁴ This would be the case for most tropical landmasses since their dry seasons would be about the same (i.e., near zero), and their wet seasons would be markedly different due to the strong diurnal cycle in convection usually present over land.

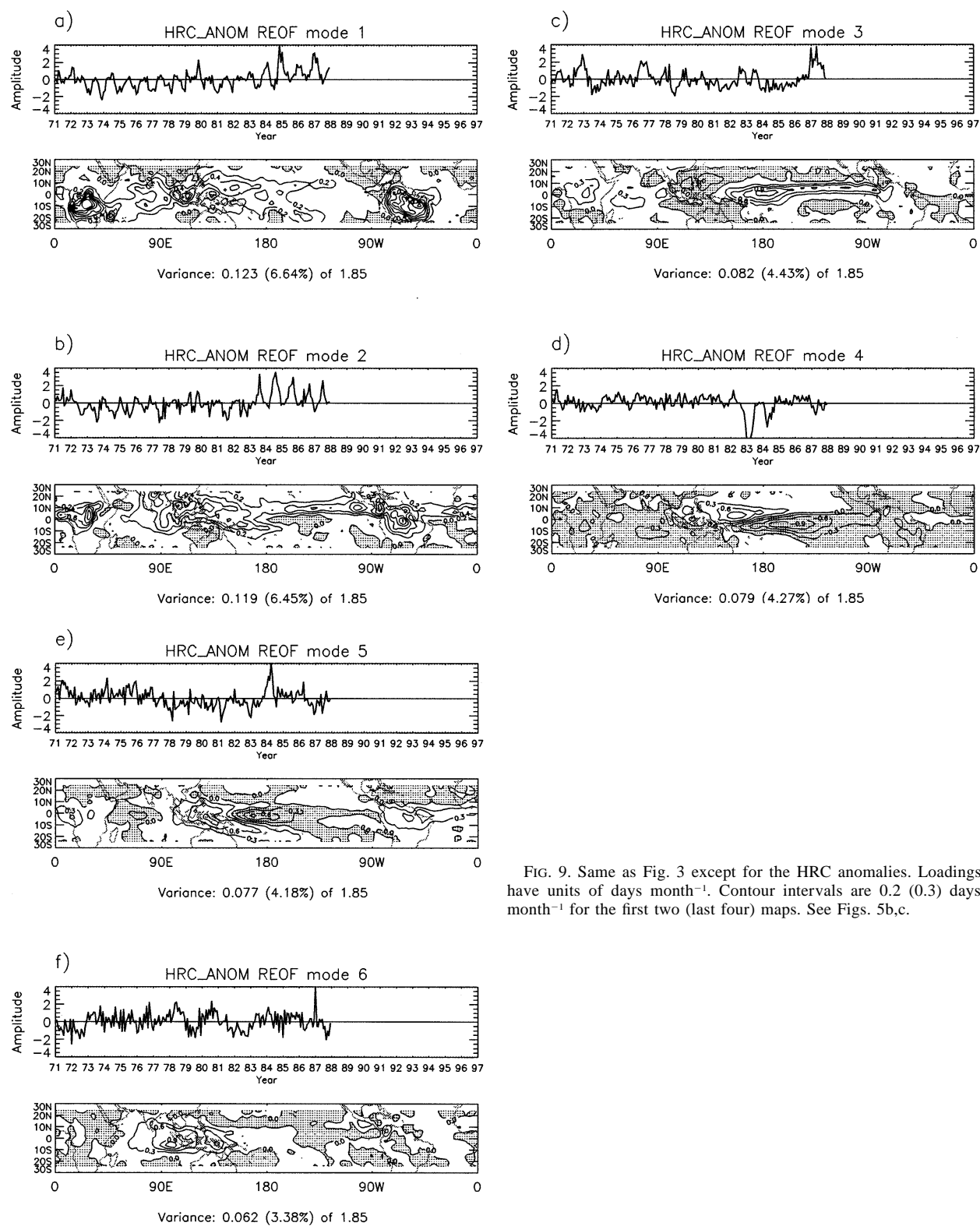


FIG. 9. Same as Fig. 3 except for the HRC anomalies. Loadings have units of days month⁻¹. Contour intervals are 0.2 (0.3) days month⁻¹ for the first two (last four) maps. See Figs. 5b,c.

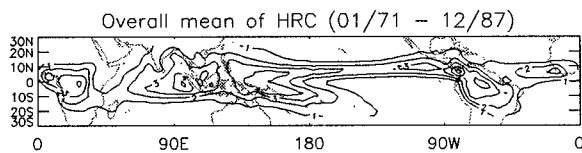


FIG. 10. Long-term mean HRC distribution (days month⁻¹).

American landmasses compared to their signs over the Pacific Ocean. The fifth mode (Fig. 9e) accounts for 4.2% of the anomaly variance. It has a spatial pattern very similar to the second OLR mode before the bias removal (Fig. 3b) and is, therefore, mostly associated with ENSO variability, in this case, especially the 1984 La Niña event.

The sixth mode (Fig. 9f), which accounts for 3.4% of the anomaly variance, has mostly very small loadings over the whole of the Tropics, except for a strong positive loading center in the eastern Indian Ocean. This feature suggests that this mode may be related to Asian monsoon variability over this area. Indeed, the weak (1979, 1982, 1983, and 1987) and strong (1984, 1985, and 1986) monsoon years, as indicated in Webster and Yang (1992), appear to be captured fairly well by the associated time series.

The above analysis indicates that the first two modes of HRC are those primarily related to changes in satellite ECT. These two modes account for 13.1% of the anomaly variance of HRC. This implies that biases caused by satellite ECT changes are relatively larger in the HRC than in the OLR, necessitating their removal for inter-annual variability and other climate studies.

d. HRC bias removal

The analysis in the previous section suggests that the two modes identified as being satellite modes are mainly related to morning or afternoon ECTs. Thus, to simplify the process of removing the satellite-related bias, the satellite ECT can be regarded as a binary variable (A.M. or P.M. only). Despite the differences between different A.M. or P.M. ECTs (e.g., 1430 versus 1530 LST) or the slow drift of the ECTs (e.g., Fig. 2), this discrete categorization will be shown to account for most of the error related to the satellite ECT in the HRC dataset. Along these lines, satellites are grouped according to morning or afternoon ECTs, respectively. Then the mean cycles of the REOF time series over the 12-month calendar (hereafter referred to as annual oscillation, as opposed to the climatological annual cycle, which has been removed) for the morning and afternoon groups are calculated separately for the time series of the first two modes (satellite modes; Figs. 9a,b). For example, the mean annual oscillation of the morning group for mode 1 was calculated from REOF time series when the satellite ECT was in the morning, such as when the NOAA SR series and NOAA-6 were operational. The four resulting 12-month cycles, A.M. and P.M. cycles for mode

1 and mode 2, respectively, are then used to reconstruct new series according to the corresponding satellite ECT (morning or afternoon) and the month of the year. The resulting reconstructed time series for the two modes are shown as the thick gray lines in Fig. 11. Also shown in Fig. 11 are the original HRC REOF time series as thin lines. Similar to the OLR case, the reconstructed time series (thick gray lines in Figs. 11a,b) are used to multiply the associated spatial patterns (Figs. 9a,b). The sum of these two modes is an estimate of the variability related to the changes of the satellite ECT and is subtracted from the total HRC anomaly dataset to produce a new, bias-removed HRC dataset.

The above bias-removal procedure needs a timetable of satellites used in the HRC derivation and their associated ECTs. As mentioned earlier, during some periods when there were more than one operational satellite, it is uncertain which satellite was used to derive the HRC data. Fortunately, these periods are limited and only account for a small fraction of the whole data record. Because the satellite ECT is considered a binary variable in this procedure, we only need to distinguish whether a morning or afternoon equatorial crossing satellite was used in deriving the HRC data. In this study, we assume that the correct satellite information will maximize our ability to capture the satellite-related bias and to subsequently remove the biases via the above procedure.

The first guess at the satellite timetable for deriving the HRC was based primarily on Garcia (1985), except for modifications for the period from January 1971 to May 1974, when information in Table 1 overrides that in Garcia (1985) (because of the inaccuracy mentioned in section 2). Using this initial table, the above bias removal procedure was applied. We found that the reconstructed time series of both modes matched well with the original (i.e., using plots similar to Fig. 12, not shown), except for some periods when there were both A.M. and P.M. operational satellites. For example, from 16 July 1979 to 27 February 1981, both *TIROS-N* (afternoon ECT) and *NOAA-6* (morning ECT) were operational. From 24 August 1981 to 20 June 1983, both *NOAA-6* and *NOAA-7* (afternoon ECT) were operational. This first guess of the HRC derivation timetable was then modified only for the periods when there was more than one operational satellite and the satellite ECT (A.M. or P.M.) used could be ambiguous. Adjustments were made so that the agreement between the reconstructed and the original time series was greatest within the constraints of the available satellite information. In fact, it was this procedure that led to the initial deduction that *ITOS-1*, *ESSA-9*, and *NOAA-1* were actually afternoon ECT satellites and not morning satellites as the HRC atlas indicates. The relatively large number of these types of unknowns with respect to the HRC ECT information (e.g., which satellite was used and what its exact crossing time was) compared to those for OLR, along with the need to describe a more complex bias

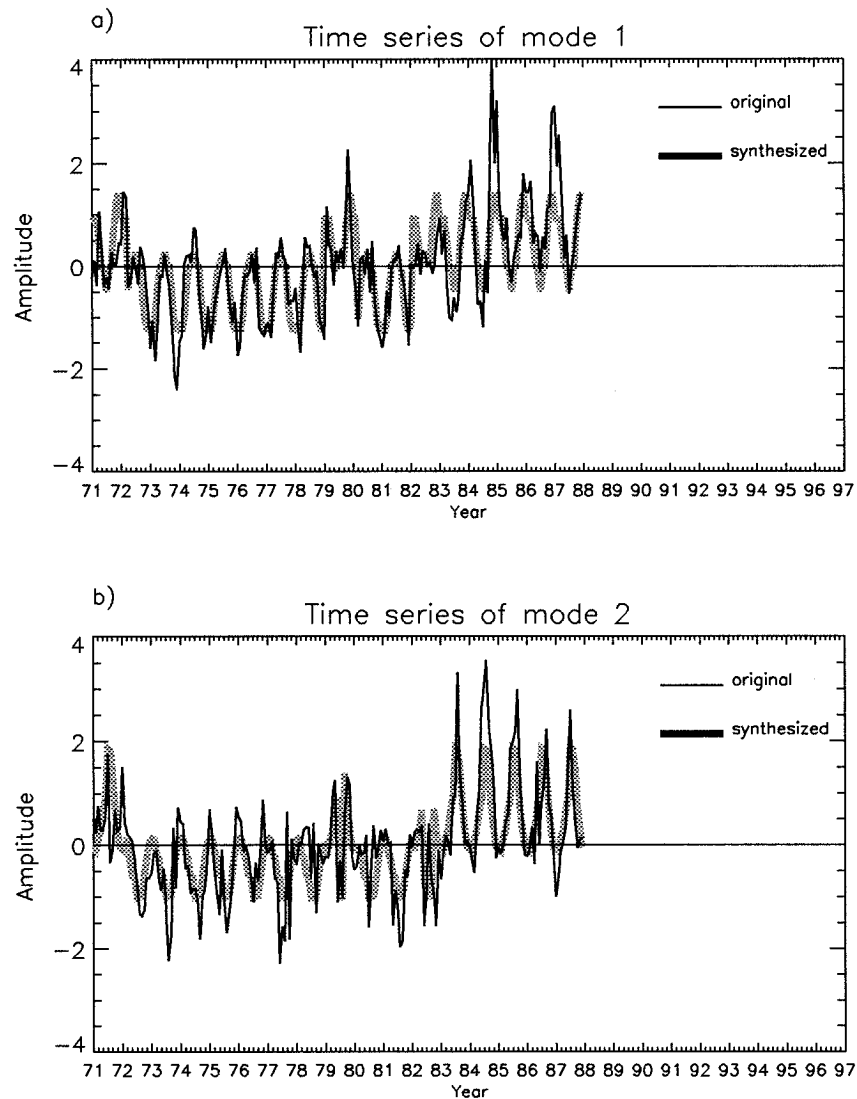


FIG. 11. Time series (thick gray lines) constructed by applying the A.M. or P.M. mean 12-month cycle based on morning or afternoon satellite ECT and month of year for the HRC REOF modes (a) 1 and (b) 2. The original time series are also plotted as thin lines (same as Figs. 9a,b).

relationship for HRC (i.e., an offset according to time of day on top of a stronger 12-month modulation) than for OLR (i.e., an offset according to time of day alone), inhibited us from tackling a more rigorous bias-removal method that may have included variations of ECT within the morning or afternoon categories (i.e., ECT drift).

Table 3 is the estimated satellite timetable based on the above analysis and adjustment procedure. Periods when the satellite used for the HRC derivation is different from that specified in Garcia (1985) are indicated. For example, during period from November 1972 to May 1974, the HRC could have only been derived from NOAA-2 or NOAA-3 instead of *ITOS-1*, *ESSA-9*, and NOAA-1 as stated in Garcia (1985). In addition, the large drift associated with *ESSA-9* (Fig. 2) induced a change in ECT time that led to it having significantly better

agreement if the last 7 months of its lifetime were categorized as a morning crossing time (i.e., about 6:00 A.M.). Further, during the period from July 1979 to August 1979, both *TIROS-N* and NOAA-6 were operational (Table 1), and thus NOAA-6 may have been used instead of *TIROS-N*, while from September 1981 to January 1982 and from June 1982 to September 1982, both NOAA-6 and NOAA-7 were operational, and thus NOAA-6 may have been used instead of NOAA-7 (O. Garcia 1996, personal communication). In each of these last three overlapping cases, the analysis indicated a different satellite (ECT) than was specified in Garcia (1985) (see Table 3).

As mentioned above, the reconstructed time series from the above bias-removal procedure based on the estimated HRC satellite timetable in Table 3 are shown

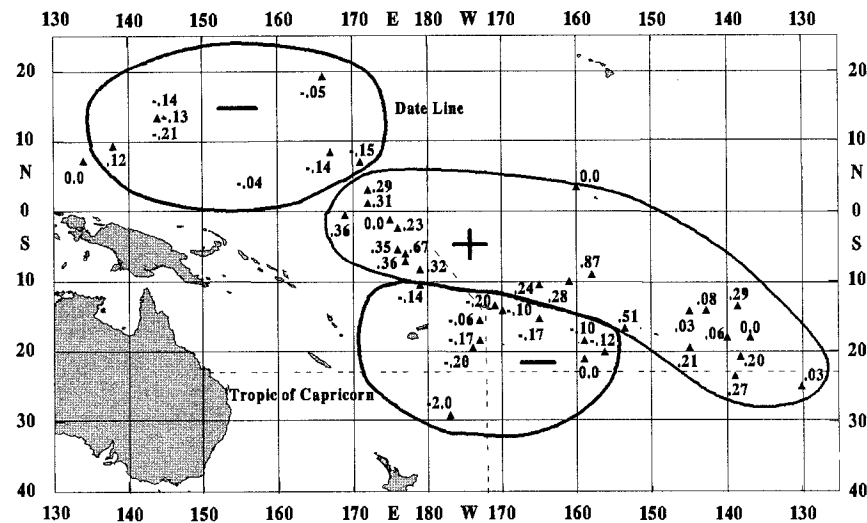


FIG. 12. Map of linear trends in rain gauge measurements between 1971 and 1990. Values are in mm month^{-1} . From Morrissey and Graham (1995).

in Fig. 11 in thick gray lines. The original time series of the first two modes are also shown in Fig. 11 as thin lines. It can be seen that the two synthesized curves (thick) are in fairly close agreement with the time series of the first two modes (thin lines). The correlations between the synthesized series and original series are 0.78 and 0.75 for mode 1 and mode 2, respectively. The modified HRC dataset is produced by the bias removal procedure mentioned above, and EOF and REOF analyses are performed. To avoid redundancy, the resulting REOF modes are not shown; however, the correlations between the time series prior to and after the bias removal are listed in Table 6.

After the bias removal, the total anomaly variance changes from 1.85 to 1.70 (days month^{-1})². From Table 6, we can see that after the bias removal, the first mode is actually the fifth mode prior to bias removal, the second mode corresponds to the third mode prior to bias removal, the third mode corresponds to the fourth mode prior to bias removal, and the sixth mode corresponds to the eighth mode prior to bias removal. Their spatial patterns (not shown) also have a near one-to-one cor-

respondence. The fourth, seventh, and eighth modes, from Table 6, are a redistribution of variances associated with the prior sixth and seventh modes and to a minor extent the second mode. Again, note the weak correlation of all the modes after the bias removal with the satellite modes 1 and 2 before the bias removal.

5. Discussion

a. OLR and HRC bias differences

It is apparent from Figs. 3d and 9a,b (or Figs. 5a–c) that the satellite ECT biases do not appear the same way in the OLR and HRC datasets. The satellite modes appear in the HRC as the first two modes, which account for 13.1% of the anomaly variance, while in the OLR, the satellite mode appears as the fourth mode, which accounts for 4.4% of the anomaly variance. This means that the HRC dataset is more severely contaminated by satellite biases. Apart from the difference of relative magnitude of the bias, the time series and spatial patterns of the OLR and HRC satellite modes do not share

TABLE 6. Correlation of HRC REOF time series before and after bias removal. Correlations greater than 0.3 are shaded.

Mode no.	Before							
	1	2	3	4	5	6	7	8
After								
1	−0.30	−0.07	0.03	−0.04	−0.79	−0.26	0.00	−0.05
2	0.13	0.11	0.95	0.07	−0.10	0.00	0.03	0.00
3	0.04	0.02	0.02	−0.97	0.03	0.00	−0.02	−0.05
4	0.06	−0.31	0.10	−0.09	0.09	−0.66	0.23	−0.15
5	0.14	−0.04	−0.05	0.01	−0.29	0.05	−0.78	−0.12
6	−0.05	−0.22	0.09	−0.11	−0.04	0.13	−0.08	0.90
7	−0.09	0.04	−0.06	0.14	0.22	−0.50	−0.12	0.25
8	−0.09	−0.15	−0.02	0.03	−0.19	0.43	0.45	−0.10

resemblance either. The spatial patterns in the two HRC satellite modes have a distinct feature of large loadings over landmasses and warm pool regions, which is different from the corresponding OLR satellite mode. The time series of HRC satellite modes show variations of two annual-scale oscillations related to morning and afternoon ECTs, while no annual oscillatory behavior is evident in the time series of the OLR satellite mode. These differences can be explained by considering the differences in the sampling and radiometric characteristics of the OLR and HRC datasets.

First, taking the OLR diurnal cycle in Sahara shown in Fig. 6 as an example shows that the difference in OLR measured at 0800 and 1500 LST can be over 30 W m^{-2} (Fig. 6, top), but the difference of the average OLR of two measurements at a 12-h interval—for example, the difference between the average of measurements at 0800 and 2000 and the average at 0300 and 1500 LST—is only about 8 W m^{-2} . Similar results should hold for the HRC as well, especially in regions in which the diurnal cycle is significant. Since only daytime measurements were used in the HRC derivation but twice per day measurements were used to derive the OLR, the difference between morning and afternoon ECT measurements is relatively larger in the HRC than that in the OLR; that is, satellite ECT change will cause a relatively larger bias in the HRC than in the OLR. Also, because the convective diurnal cycle over land is usually stronger than over sea, morning and afternoon satellite ECT changes will produce a larger artificial variation over land and, thus, result in a large difference in spatial loadings between land and ocean, as is observed in the HRC.

Second, there is a fundamental difference between the quantities measured by the HRC and OLR. HRC is only an indication of presence of deep convective clouds. No other cloud type or process is represented in the HRC. Thus, in the HRC, due to higher convective probabilities in the afternoon (typically observed over land areas), morning observations of the climate (e.g., the annual cycle) will have consistently lower values than the afternoon observations. As described in Eqs. (1)–(5), removing the long-term mean annual cycle to produce the HRC anomalies still leaves annual-scale residual oscillations for morning and afternoon observation periods and the residual oscillations will be 180° out of phase. In fact, as shown in Fig. 11, the oscillations in the time series for morning and afternoon satellite ECTs are about 6 months out of phase. This, in conjunction with the overall north–south offset in the associated convection patterns, combines to describe the (annual scale) oscillation that leads to the overall apparent increase or decrease of the true annual cycle brought about by a change in the sampling time (section 4c). In contrast, OLR is primarily determined by either cloud-top temperature, if clouds are present, or by the earth's surface temperature, as well as the water vapor content in the atmosphere, if the sky is clear. Because

of the presence of both conditions over time, the monthly OLR is a mixture of high-temperature surface emission and low-temperature cloud-top emission. Typically, since convection is stronger (e.g., lower cloud-top temperature) and surface temperature is higher in the afternoon than in the morning, the afternoon OLR emission is from either a cloud top that is colder than in the morning or a surface that is warmer than in the morning. Thus, mixing emissions from cloud top and surface to form the monthly OLR will to some extent cancel out the distinct difference between morning and afternoon measurements. Also, OLR measurements are dominated by afternoon ECT satellites and are observed twice per day at 12-h intervals, the latter providing a better estimate of the daily average. All these factors contribute to the fact that no annual-scale oscillation occurs in the first few OLR REOF modes as it does for the HRC after the long-term mean annual cycle is removed.

The above analysis has shown that both the OLR and HRC datasets are subject to biases resulting from changes in the satellite ECT. However, after bias removal, the REOF modes of these two datasets have a much closer correspondence. This is to be expected since the OLR and HRC are both widely considered to be indicators of convective activity in the Tropics, and it also suggests that the bias-removing methods developed in this study are reasonably effective.

b. Tropical climate trend

As mentioned in the introduction, OLR has been used in a number of studies that indicate a decadal-scale trend in convection–precipitation in the tropical western-central Pacific during the 1970s and 1980s (e.g., Nitta and Yamada 1989; Graham 1995; Morrissey and Graham 1996). However, in each case, the confidence that can be attributed to the computed trends is diminished by the presence of sensor and satellite ECT changes that occur within the OLR data (e.g., Table 1). In addition to OLR data, Morrissey and Graham (1996) analyzed rain gauge data between 1971 and 1990, and found a trend and spatial loading pattern consistent with the spatial pattern of the OLR trend. Their trends in rain gauge data are shown in Fig. 12. Maximum values in the western–central tropical Pacific are about $0.3\text{--}0.5 \text{ mm month}^{-1}$, which is equivalent to an increase in monthly precipitation of about 72–120 mm over the 20-yr record. Morrissey and Graham (1996) also showed downward trends of OLR from -0.10 to $-0.18 \text{ W m}^{-2} \text{ month}^{-1}$ over the same region, which represents a decline of about -17 to -30 W m^{-2} during the 14-yr period between June 1974 and December 1987. While sampling from rain gauges has its own difficulties (Morrissey et al. 1995), the agreement between the rain gauge and OLR data provides additional support that such a trend is not an artifact of the data being analyzed (cf. Flohn et al. 1990; Gutzler 1992; Gaffen et al. 1991; Oort and Liu 1993).

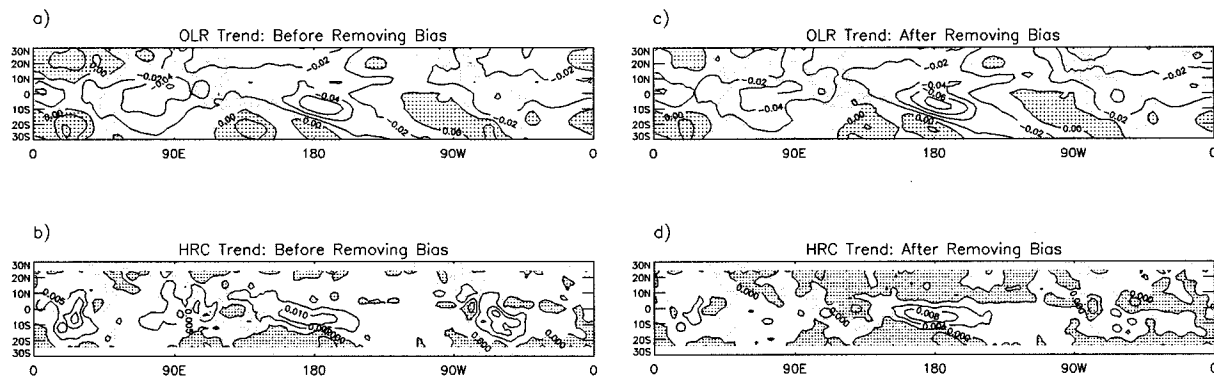


FIG. 13. Maps of linear trends in the OLR and HRC datasets (a) and (b) before and (c) and (d) after the ECT bias-removing procedures have been applied. Shading indicates positive (negative) trends in OLR (HRC), with units are in $\text{W m}^{-2} \text{ month}^{-1}$ (days month^{-2}). Contour intervals are (a) 0.02, (b) 0.005, (c) 0.02, and (d) 0.004.

In the interest of understanding how the satellite ECT biases may affect the trends found in the OLR and HRC data, we have computed the linear trend at each spatial point in the OLR and HRC before and after the biases have been removed. Figures 13a and 13b show the trends in the OLR and HRC data, respectively, before the bias removal. Note that the shading indicates positive (negative) trends for the OLR (HRC). In each case, there is evidence that the ECT modes are adversely affecting the trend calculation. The spatial pattern of the OLR trend bears some resemblance to the OLR ECT mode (Fig. 3d), indicating that the time series associated with that particular mode has an overall (decreasing) trend. The spatial pattern of the HRC trend indicates an overall increase in convection with a pattern similar to the mean, and thus it also exhibits artificial changes due to its ECT modes (Figs. 9a,b). However, in both the uncorrected OLR and HRC cases, there is a signature of a trend in the western-central Pacific that is similar to the rain gauge trends shown in Fig. 12, although distinguishing these from the ECT biases is somewhat difficult.

Figures 13c and 13d (see Figs. 5d,e) show the trends in the OLR and HRC data, respectively, after the bias removal. As expected, the bias-removal procedures diminishes the effects from the ECT modes on the trend. In addition, the bias removal leaves a more pronounced feature in the western-central Pacific, which shows a rather close spatial correspondence to the rain gauge trends shown in Fig. 12. The values of the trends in these regions are about $-0.08 \text{ W m}^{-2} \text{ month}^{-1}$ and $0.01 \text{ days month}^{-2}$. These correspond to a decrease of 21 W m^{-2} over the 266-month OLR record and an increase of $2.0 \text{ days month}^{-1}$ over the 204-month HRC record. Previous studies comparing OLR and HRC directly (Waliser et al. 1993) or comparing how they each vary with SST (Waliser and Graham 1993) show that, in general, a $8\text{--}10 \text{ W m}^{-2}$ OLR change is roughly equivalent to a 1 day month^{-1} HRC change. Thus, the trends in the HRC and OLR for the western-central Pacific tend to be in reasonable agreement with respect to their

spatial patterns and magnitudes. Note that the two datasets do not overlap, so neither trend appears to be inherently tied to end points within one dataset or the other.

Comparison to the trends in the rain gauge data can be made by considering the regression relation between tropical Pacific rainfall (Coral Island) and HRC computed by Kilonsky and Ramage (1976), which suggests that a 1 day month^{-1} HRC change is equivalent to 39 mm month^{-1} . Converting the HRC trend over the period 1971–87 using this relation gives $0.4 \text{ mm month}^{-1}$, or about 80 mm total increase over the period. These values correspond closely to the trends observed directly from the rain gauges between 1971 and 1990. The above agreement in the spatial patterns and magnitudes of the trends in the three different rainfall indices, HRC, OLR, and rain gauges, strongly suggest that the decadal trend observed in this area of the Tropics is distinct from the satellite ECT biases and, in fact, appears to be independent of the instruments or measurement techniques pertaining to the three rainfall indices.

6. Summary

The objective of this study is to examine the impacts from satellite ECT changes on the OLR and HRC datasets and to design appropriate and robust methods to remove these satellite-dependent biases. Rotated empirical orthogonal function analysis is performed on both the monthly OLR and HRC anomalies to help distinguish between artificial modes of variability and those associated with real variability. Results from the analysis show that significant errors are introduced by changes in the satellite ECT, and they appear differently in the two datasets. The primary satellite-related bias in the OLR appears as the fourth REOF mode and accounts for 4.4% of the OLR anomaly variance. Its spatial pattern exhibits a strong surface signature over land, with the opposite sign over many of the deep convective regions of the ocean. During some periods, these biases result in widespread errors of over 10 W m^{-2} , which

are sustained for several months to over a year. In other cases, the transitions between satellites (e.g., from *NOAA-12* to *NOAA-14*) induce abrupt, artificial changes in the OLR as high as 16 W m^{-2} . In the HRC, the satellite-related bias appears as the leading two REOF modes, which account for 13.1% of the HRC anomaly variance. The spatial patterns of the HRC biases are indicative of an overall change to the mean climatological convection pattern, while the two REOF time series show annual-scale oscillations with phase differences between periods of morning and afternoon satellite ECTs. These results can be understood by considering the sampling and radiometric characteristics of the OLR and HRC datasets, as discussed in sections 4 and 5a.

To remove the satellite ECT biases, the time series of the satellite-related modes are reconstructed by using detailed knowledge of the satellite ECTs so that, to the extent possible, only the artificial variability related to satellite ECT changes is captured and the natural variability is excluded. For OLR, since the bias has a close relationship with the satellite ECT, the time series is reconstructed based on a polynomial fit of the satellite mode time series with the exact satellite ECTs. For HRC, the primary biases are shown mainly as annual-scale oscillations with systematic difference between morning and afternoon ECT periods. In this case, the time series are reconstructed by compositing the mean annual-scale oscillations of the satellite modes' time series from periods associated with morning and afternoon ECT, respectively. These reconstructed time series, for both the OLR and HRC, are then used in conjunction with the associated spatial patterns to compute the satellite ECT biases, which are removed from the datasets.

The revised datasets represent a marked improvement over the originals and provide an improved resource to study intraseasonal and longer timescale regional climate variations, large-scale interannual variability, and global-scale climate trends. For example, the leading two HRC REOF modes in the revised dataset represent interannual variability instead of nonphysical biases. In addition, the revised OLR and HRC datasets are shown to have much better consistency over the Tropics, with their leading REOF modes having a near one-to-one correspondence. Furthermore, analyses of the long-term trends in both datasets show that the satellite biases induce artificial trends in the data and that these artificial trends are reduced in the corrected datasets. Finally, the trends that do remain in the corrected datasets imply an increase in precipitation in the tropical western-central Pacific that appears to be spatially independent of the satellite biases and agrees with results of previous studies employing rain gauge data over a similar period (e.g., Morrissey and Graham 1996).

Acknowledgments. Support for this research was provided by the National Oceanic and Atmospheric Administration's Pan American Climate Study Program Grant NA56GP0236. The authors would like to thank

John E. Janowiak of the Climate Analysis Center/NWS/NOAA, Oswaldo Garcia of San Francisco State University, and Arnold Gruber and Lee Ranne of the NOAA/NESDIS for providing detailed NOAA polar orbit satellite information, as well as Michael B. Richman of the Department of Meteorology, University of Oklahoma, for helpful discussions regarding rotated EOF analysis. The authors would also like to thank the two anonymous reviewers for providing many helpful suggestions that improved the presentation of the article, and Dr. Mark Morrissey for kindly providing a copy of Fig. 12. This study's analysis greatly benefited from the use of the TeraScan software analysis system, a product of SeaSpace Corporation of San Diego.

APPENDIX

EOF Significance Test

In order to determine the number of modes to keep in the EOF rotations, we applied the N-rule significance test developed by Preisendorfer et al. (1981). An example of its application to cyclone frequency data can be found in Overland and Preisendorfer (1982). In the N-rule test, a dataset of random numbers with the same dimensions in time (N points) and space (P points) is produced and then the EOF procedure is performed. The eigenvalue percentages (i.e., the percentage of the total anomaly variance described by an eigenvalue) are then sorted in descending order, giving a mode 1 value, a mode 2 value, . . . , and finally a mode P value. This procedure is performed on 100 different random datasets. The eigenvalue percentages for each mode (1, . . . , P) are then sorted in descending order. This will give a list of 100 mode 1 eigenvalue percentages, 100 mode 2 eigenvalue percentages, . . . , and finally a list of 100 mode P eigenvalue percentages, each in descending order. The first eigenvalue percentage in each list denotes a 99% significance level, the fifth eigenvalue percentage in each list denotes a 95% significance level, etc. The inference is that if a particular eigenvalue percentage, say the mode 1 value, from an observed dataset exceeds the largest mode 1 eigenvalue percentage obtained from 100 random datasets, then with at least 99% confidence, it can be said to be significantly different than random noise.

The above procedure was performed for both the OLR and HRC datasets. However, in the interest of making a conservative estimate, an attempt was made to determine the actual number of independent samples in time and space (i.e., N and P) for each dataset. For the case of the OLR, N_{OLR} equals 266 (months) and P_{OLR} equals 3600 (144×25) spatial points. However, the autocorrelation computed in the zonal direction at each meridional point, averaged over time, suggests a decorrelation scale ($1/e$) as large as 20° (~ 8 points). Likewise, the autocorrelation computed in the meridional direction at each zonal point, averaged over time, suggests a de-

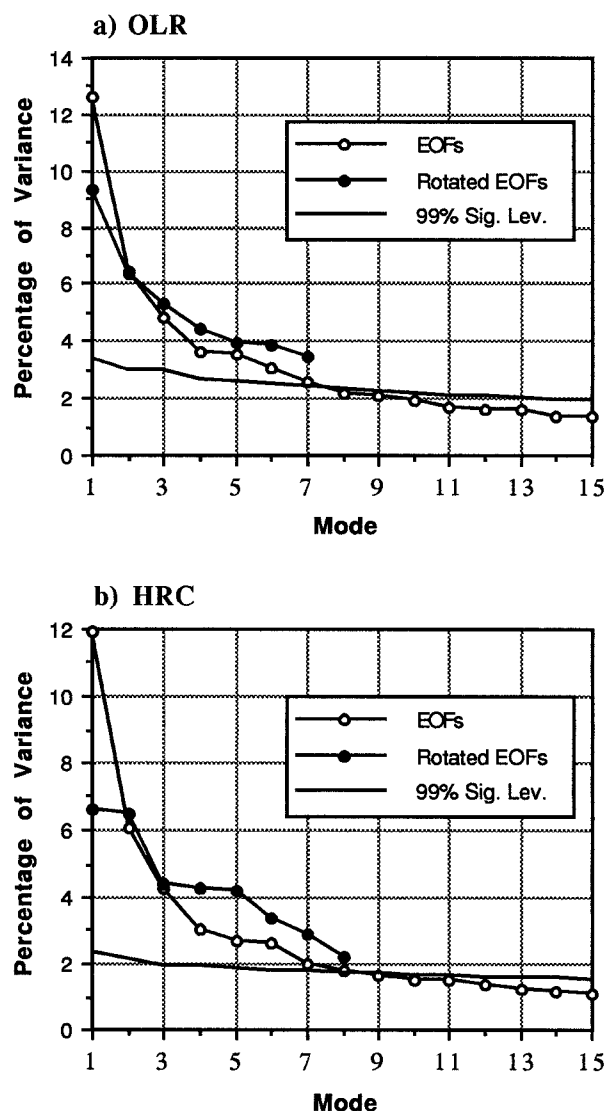


FIG. A1. Eigenvalues, in terms of percentages of anomaly variance explained, from the (a) OLR and (b) HRC EOF decompositions (open circles), along with estimated values of their 99% confidence limits (solid lines). See discussion in the appendix and section 3. Also shown for comparison purposes are the eigenvalues of the REOFs.

correlation scale as large as 7.5° (~ 3 points). Together, these two factors reduce P_{OLR} from 3600 to 144 (18×8). The autocorrelation computed in the temporal direction at each spatial point, averaged over the meridional direction, suggests that the decorrelation scale is just under 2 months. Again, in the interest of a conservative estimate, we assume 2 months and reduce N_{OLR} to 133. Similar procedures for the HRC give a decorrelation scale of 8.0° (~ 4 points) in the zonal direction, 4.0° (~ 2 points) in the meridional direction, and a near-2-month decorrelation in time. These values reduce P_{HRC} and N_{HRC} to 540 (45×12) and 102, respectively. For a discussion regarding the differences in decorrelation

scales between the OLR and HRC, see Waliser et al. (1993).

Based on the above N and P values for OLR and HRC, N-rule significance tests were performed. Figure A1 shows the results of the test. The solid thin lines in the plots show the 99% confidence limits. The lines with open circles show the eigenvalue percentages from the OLR (Fig. A1a) and HRC (Fig. A1b) EOF decompositions. For the OLR (HRC), the first seven (eight) modes are judged to be significant by the 99% confidence limit and, thus, were the modes included in the EOF rotation procedure (sections 4a and 4c). For comparison purposes, the plots also show the eigenvalue percentages for the rotated modes (lines with filled circles).

REFERENCES

- Chelliah, M., and P. Arkin, 1992: Large-scale interannual variability of monthly outgoing longwave radiation anomalies over the global tropics. *J. Climate*, **5**, 371–389.
- Flohn, H., A. Kapala, H. R. Knoche, and H. Michel, 1990: Recent changes of the tropical water and energy budget and of mid-latitude circulations. *Climate Dyn.*, **4**, 237–252.
- Gadgil, S., A. Guruprasad, and J. Srinivasan, 1992: Systematic bias in the NOAA outgoing longwave radiation dataset? *J. Climate*, **5**, 867–875.
- Garcia, O., 1985: *Atlas of Highly Reflective Clouds for the Global Tropics: 1971–1983*. U.S. Department of Commerce, NOAA, Environmental Research Laboratory, 365 pp.
- Gill, A. E., and E. M. Rasmusson, 1983: The 1982–83 climate anomaly in the equatorial Pacific. *Nature*, **305**, 229–234.
- Graham, N. E., 1995: Simulation of recent global temperature trends. *Science*, **267**, 666–671.
- , and T. P. Barnett, 1987: Sea surface temperature, surface wind divergence, and convection over tropical oceans. *Science*, **238**, 657–659.
- Gruber, A., and J. S. Winston, 1978: Earth-atmosphere radiation heating based on NOAA scanning radiometer measurements. *Bull. Amer. Meteor. Soc.*, **59**, 1570–1573.
- , and A. F. Krueger, 1984: The status of the NOAA outgoing longwave radiation data set. *Bull. Amer. Meteor. Soc.*, **65**, 958–962.
- , and T. S. Chen, 1988: Diurnal variation of outgoing longwave radiation. *J. Climatol.*, **8**, 1–16.
- Gutzler, D. S., 1992: Climatic variability of temperature and humidity across the tropical western Pacific. *Geophys. Res. Lett.*, **19**, 1595–1598.
- , and T. M. Wood, 1990: Structure of large-scale convection anomalies over tropical oceans. *J. Climate*, **3**, 483–496.
- Harrison, E. F., P. Minnis, B. R. Barkstrom, V. Ramanathan, R. D. Cess, and G. G. Gibson, 1990: Seasonal variation of cloud radiative forcing derived from the Earth Radiation Budget Experiment. *J. Geophys. Res.*, **95**, 18 687–18 703.
- Hartmann, D. L., V. Ramanathan, A. Berroir, and G. E. Hunt, 1986: Earth radiation budget data and climate research. *Rev. Geophys.*, **24**, 439–468.
- Hastenrath, S., 1990: The relationship of highly reflective clouds to tropical climate anomalies. *J. Climate*, **3**, 353–365.
- Hendon, H. H., and K. Woodberry, 1993: The diurnal cycle of tropical convection. *J. Geophys. Res.*, **98**, 16 623–16 637.
- Horel, J. D., 1981: A rotated principal component analysis of the Northern Hemisphere 500-mb height field. *Mon. Wea. Rev.*, **109**, 2080–2092.
- Johnson, J. D., F. C. Parmenter, and R. Anderson, 1976: Environ-

- mental satellites: Systems, data interpretation, and applications. NOAA/NESS, Washington, DC, 66 pp.
- Kayano, M. T., V. E. Kousky, and J. E. Janowiak, 1995: Outgoing longwave radiation biases and impacts on empirical orthogonal function modes of interannual variability in the Tropics. *J. Geophys. Res.*, **100**(D2), 3173–3180.
- Kilonsky, B. J., and C. S. Ramage, 1976: A technique for estimating tropical open-ocean rainfall from satellite observations. *J. Appl. Meteor.*, **15**, 972–976.
- Kondragunta, C. R., and A. Gruber, 1994: Diurnal variation of the ISCCP cloudiness. *Geophys. Res. Lett.*, **21**, 2015–2018.
- , and —, 1995: Spurious semi-diurnal variation in the E.R.B.E. outgoing longwave radiation. NOAA Tech. Rep. NESDIS 84, 24 pp.
- Lau, K. M., and P. H. Chan, 1988: Intraseasonal and interannual variations of tropical convection: A possible link between the 40–50 day oscillation and ENSO? *J. Atmos. Sci.*, **45**, 506–521.
- Madden, R. A., and P. R. Julian, 1972: Description of global-scale circulation cells in the tropics with a 40–50 day period. *J. Atmos. Sci.*, **29**, 1109–1123.
- Morrissey, M. L., and N. E. Graham, 1996: Recent trends in rain gauge precipitation measurements from the tropical Pacific: Evidence for an enhanced hydrologic cycle. *Bull. Amer. Meteor. Soc.*, **77**, 1207–1219.
- , M. A. Shafer, S. E. Postawko, and B. Gibson, 1995: The Pacific rain gauge rainfall database. *Water Resour. Res.*, **31**, 2111–2113.
- Murakami, T., L.-X. Chen, A. Xie, and M. L. Shrestha, 1986: Eastward propagation of 30–60 day perturbations as revealed from outgoing longwave radiation data. *J. Atmos. Sci.*, **43**, 961–971.
- Nitta, T., and S. Yamada, 1989: Recent warming of the tropical sea surface temperature and its relationship to the Northern Hemisphere circulation. *J. Meteor. Soc. Japan*, **67**, 375–383.
- Oort, A. H., and H. Liu, 1993: Upper-air temperature trends over the globe, 1958–1989. *J. Climate*, **6**, 292–307.
- Overland, J. E., and R. W. Preisendorfer, 1982: A significance test for principal components applied to a cyclone climatology. *Mon. Wea. Rev.*, **110**, 1–4.
- Philander, S. G., 1991: *El Niño, La Niña, and the Southern Oscillation*. Academic Press, 293 pp.
- Preisendorfer, R. W., F. W. Zwiers, and T. P. Barnett, 1981: Foundations of principal component selection rules. Scripps Institution of Oceanography Rep. 81-7, 200 pp.
- Ramage, C. S., and A. M. Hori, 1981: Meteorological aspects of El Niño. *Mon. Wea. Rev.*, **109**, 1827–1835.
- Rao, P. K., S. J. Holmes, R. K. Anderson, J. S. Winston, and P. E. Lehr, 1990: *Weather Satellites: Systems, Data, and Environmental Applications*, P. K. Rao, S. J. Holmes, R. K. Anderson, J. S. Winston, and P. E. Lehr, Eds., Amer. Meteor. Soc., 7–201.
- Rasmusson, E. M., and J. M. Wallace, 1983: Meteorological aspects of the El Niño/Southern Oscillation. *Science*, **222**, 1195–1202.
- Reynolds, R. W., 1988: A real-time global sea surface temperature analysis. *J. Climate*, **1**, 75–86.
- Richman, M. B., 1986: Rotation of principal components. *J. Climatol.*, **6**, 293–335.
- , and P. J. Lamb, 1985: Climatic pattern analysis of 3- and 7-day summer rainfall in central United States: Some methodological considerations and a regionalization. *J. Climate Appl. Meteor.*, **24**, 1325–1343.
- Ropelewski, C. F., and M. S. Halpert, 1987: Global and regional scale precipitation patterns associated with the El Niño/Southern Oscillation. *Mon. Wea. Rev.*, **115**, 1606–1626.
- , and —, 1989: Patterns associated with the high index phase of the Southern Oscillation. *J. Climate*, **2**, 268–284.
- Rossow, W. B., and R. A. Schiffer, 1991: ISCCP cloud data products. *Bull. Amer. Meteor. Soc.*, **72**, 2–20.
- Spencer, R. W., 1993: Global oceanic precipitation from the MSU during 1979–91 and comparisons to other climatologies. *J. Climate*, **6**, 1301–1326.
- Waliser, D. E., and C. Gautier, 1993: A global climatology of the ITCZ. *J. Climate*, **6**, 2162–2174.
- , and N. E. Graham, 1993: Convective cloud systems and warm-pool SSTs: Coupled interactions and self-regulation. *J. Geophys. Res.*, **98**(D7), 12 881–12 893.
- , —, and C. Gautier, 1993: Comparison of the highly reflective cloud and outgoing longwave radiation datasets for use in estimating tropical deep convection. *J. Climate*, **6**, 331–353.
- Webster, P. J., and S. Yang, 1992: Monsoon and ENSO: Selectively interactive systems. *Quart. J. Roy. Meteor. Soc.*, **118**, 877–926.
- Zebiak, S. E., 1990: Diagnostic studies of Pacific surface winds. *J. Climate*, **3**, 1016–1031.
- Zimmerman, P. H., H. B. Selkirk, and R. E. Newell, 1988: The relationship between large-scale vertical motion, highly reflective cloud, and sea surface temperature in the tropical Pacific basin. *J. Geophys. Res.*, **93**(D9), 11 205–11 215.